Diss. ETH No. 18318

Diffusion-Weighted MRI
–
Volume Selection, Field Monitoring and Image Reconstruction

A dissertation submitted to the

Swiss Federal Institute of Technology Zurich

for the degree of

Doctor of Sciences

presented by

Bertram Jakob Wilm
Dipl. inf. TUM
born July 4th, 1979
citizen of Germany

accepted on the recommendation of

Prof. Dr. Peter Boesiger
Prof. Dr. Spyros Kollias

Zurich, 2009

Contents

Summary

Diffusion-weighted imaging (DWI) is a powerful magnetic resonance imaging (MRI) technique to asses Brownian motion induced diffusion processes of water molecules in human tissue. DWI allows an indirect measurement of underlying tissue microstructure, enabling the investigation of pathologic changes on a microscopic level. In this context structural changes can be followed over the time course of a disease, thus providing a valuable tool to help understand the underlying pathologies, as well as to improve outcome prediction and medical treatment. At present, diffusion-weighted imaging is used as an important contribution in the diagnosis of acute ischima and is currently being investigated for the diagnosis of a variety of other diseases.

One of the key-problems in DWI is the inherently low signal-to-noise ratio, which limits it to a relatively coarse image resolution, and noise contamination in the image reduces specificity and sensitivity of diagnoses based on DWI. The limited resolution restricts the application of this method to larger pathologies and complicates the distinction of pathologic and healthy tissue respectively, which again confines the specificity and sensitivity of the method. Additionally, DWI easily suffers from motion artifacts caused by minimal physiological motion such as cardiac pulsation and respiration. The so called "single-shot" methods are relatively robust against motion artifacts, but suffer from distortions that are induced by local variation in magnetic susceptibility. Moreover, eddy currents induced into the conducting components of the MR system that arise during the DWI sequence will also lead to image distortions. In both cases it is once again necessary to constrain the image resolution.
The present dissertation is dedicated to the development of new concepts

for improving acquisition techniques for DWI, in particular to increase the feasibility of DWI in the spinal cord. As compared to DWI in the brain, the small cross-sectional area of the spinal requires a particularly high image resolution. Additionally, image acquisition is also complicated by the inhomogeneous magnetic environment, and by the pulsatile motion of the cerebrospinal fluid around the cord and the spinal cord itself. In this context, the main focus was the implementation and investigation of an MRI sequence which enables a robust DWI of the spinal cord with adequate image quality. Similar to parallel imaging techniques, a reduction in field-of-view enables to shorten the acquisition duration for single-shot sequences, thereby achieving enhanced image resolution, substantially diminished susceptibility artifacts, and an increase in signal-to-noise ratio in the data. The method is currently employed in three clinical studies for investigating spinal cord multiple sclerosis, spinal cord trauma and for the detection of prostate carcinomas.

A second aim of this work was dedicated to solving the problem of image distortions that are caused by eddy-current induced field perturbations during the DW sequence. To tackle this problem on a general level, magnetic field monitoring was employed. The actual spatial-temporal field evolution can be measured during image acquisition using NMR probes that have been recently developed at the Institute of Biomedical Engineering. The field evolution data is incorporated into image reconstruction, allowing all deviations from the desired image encoding to be corrected without relying on prior knowledge or model-based approaches. In the course of this project, the NMR-probe hardware was enhanced to achieve robust and independent excitation of the probes, which enables assessment of the field evolution during the diffusion-weighted experiments. These measurements revealed new insights into the cause and the characteristics of the magnetic field deviations, specifically that the eddy-current induced fields have considerable contributions that are non-linear in space. To correct for the resulting image distortions, an algorithm was developed that allows direct integration of higher-order dynamic fields. This approach included difficulties not only in developing new formalisms to describe these fields, but also in the numerical complexity of the image reconstruction, which can no longer depend on time efficient algorithms used for Fourier-encoded imaging. The presented method contributes to the improvement of DWI in the spinal cord by directly enhancing image acquisition for spatially limited regions (focal anatomy), as well as by developing a general method to account for deviations from the desired image encoding in diffusion-weighted imaging. Future development of these methods, and combination with existing techniques, holds the potential to open up a wide range of advances in other areas of MR imaging and spectroscopy.

Zusammenfassung

Die auf der Magnetresonanztomographie (MRT) basierende Diffusionsbildgebung ermöglicht es, die auf Grund der Brown'schen Bewegung stattfindenden Diffusionsprozesse von Wassermolekülen in menschlichem Gewebe zu erfassen. Indirekt können so Rückschlüsse auf das zugrunde liegende Gewebe gezogen werden. Insbesondere ermöglicht sie die Untersuchung von mikrostrukturellen Veränderungen, die im Zusammenhang mit verschiedensten Pathologien auftreten können. So ist die Diffusionsbildgebung unter anderem ein wichtiger diagnostischer Baustein bei akuter Ischämie (Schlaganfall) und wird derzeit für die Diagnostik vieler anderer Krankheitsbilder untersucht. Dabei können strukturelle Veränderungen während des zeitlichen Verlaufs von Krankheiten studiert bzw. überwacht werden. Die so gewonnenen Erkenntnisse leisten einen wertvollen Beitrag zum besseren Verständnis von Ursache, Prognose und Therapie dieser Krankheiten.

Eine der Hauptschwierigkeiten bei der Diffusionsbildgebung besteht darin, dass das inhärent niedrige Signal-zu-Rausch-Verhältnis in den Bilddaten nur eine relativ schlechte räumliche Auflösung zulässt. Verrauschte Daten vermindern die Spezifität und Sensitivität der auf Grundlage der Daten gestellten Diagnose. Die eingeschränkte Auflösung limitiert die Anwendung der Methode auf grössere Pathologien bzw. erschwert die Unterscheidung von gesundem und krankem Gewebe, was wiederum zu einer Einschränkung von Sensitivität bzw. Spezifität der Methode führt.
Ein zweites Problem ist, dass abhängig von der gewählten Aufnahmetechnik auch schon minimale physiologische Bewegungen (bedingt durch Herzschlag und Atmung) zu Bildartefakten führen können. Sogenannte Single Shot-Akquisitionstechniken sind relativ robust gegenüber Bewegungsartefakten, allerdings kommt es hier häufig zu Bildverzerrungen, die durch

lokale Variation der magnetischen Suszeptibilität des Gewebes ausgelöst werden. Ausserdem können Wirbelströme, die im Zuge der Diffusionsgewichtung in leitfähige Teile des MR-Tomographen induziert werden, globale Bildverzerrungen verursachen. In beiden Fällen führt dies wieder zu einer Reduzierung der erreichbaren Bildauflösung.

Die vorliegende Dissertation beschäftigt sich mit der Entwicklung neuer Konzepte für die Aufnahme und Rekonstruktion von diffusionsgewichteten MR-Bildern.
Das Ziel war es, die Diffusionsbildgebung, die sonst vorwiegend im Gehirn angewendet wird, auch im Rückenmark zu etablieren. Durch die kleine Querschnittsfläche des Rückenmarks ist eine besonders hohe Auflösung der Bilder nötig, wobei die Aufnahme zusätzlich durch das inhomogene magnetische Umfeld und durch pulsatile Bewegung des Rückenmarks erschwert wird. Schwerpunkt der Arbeit bestand hierbei in der Entwicklung und Analyse einer MR-Sequenz, die eine robuste Aufnahme des Rückenmarks ermöglicht. Ähnlich zu den parallelen MRI-Verfahren, kann durch eine Einschränkung des abzubildenden Bildausschnittes eine Verkürzung der Akquisitionsdauer für Single Shot-Aufnahmen erreicht werden. Dadurch ermöglicht man eine Verbesserung der Bildauflösung, stark verringerte suszeptibilitätsbedingte Verzerrungen, sowie einer Erhöhung des Signal-zu-Rausch-Verhältnisses in den Daten. Die Methode wird derzeit in drei klinischen Studien zur Untersuchung von spinaler Multiple Sklerose und spinalem Trauma sowie zur Detektion von Prostatakarzinomen eingesetzt.
Ein zweiter Schwerpunkt dieser Arbeit beschäftigt sich mit der Lösung der durch Wirbelströme verursachten Bildverzerrungen, welche auch die Diffusionsbildgebung in Rückenmark betrifft. Dabei kommt das sogenannte *Magnetfeld-Monitoring* zum Einsatz. Die Grundlage dafür schaffen NMR-Proben (nuclear magnetic resonance), die vor kurzem am Institut für Biomedizinische Technik der ETH entwickelt wurden. Diese ermöglichen die Messung der raumzeitlichen Feldentwicklung, die gleichzeitig mit der Bildakquisition stattfinden kann. Diese Daten werden dann zur Rekonstruktion der Bilder herangezogen. Anders als bei bisherigen Verfahren können alle Abweichungen von der angenommenen Bildkodierung miteinbezogen werden, ohne dabei auf Vorwissen bzw. modellbasierte Annahmen zurückgreifen zu müssen. Durch eine Weiterentwicklung der NMR-Proben-Hardware im Zuge dieser Dissertation, die eine robuste und unabhängige Anregung der Proben gestattet, konnten Feldevolutionen während der Dif-

fusionsbildgebungsexperimente erhoben werden. Dabei kamen neue Erkenntnisse über die Ursachen und Ausprägungen von Abweichungen gegenüber der gewünschten Bildkodierung zutage. So konnte gezeigt werden, dass die durch Wirbelströme induzierten Felder eine starke räumliche Nicht-Linearität aufweisen und einen erheblichen Teil der Bildverzerrungen verursachen. Um diese zu korrigieren, wurde ein Algorithmus entwickelt, der allgemein die Einbeziehung von zeitlich-dynamischen Feldern höherer räumlicher Ordnungen ermöglicht. Die Schwierigkeiten lagen dabei nicht nur in der Entwicklung neuer Formalismen zur Beschreibung und Integration dieser Felder, sondern auch in der numerischen Komplexität der Bildrekonstruktion, die nicht mehr auf effizienten Algorithmen für Fourier-basierte Bildkodierung zurückgreifen kann.

Die hier vorgestellten Methoden tragen zu einer Verbesserung der Diffusionsbildgebung im Rückenmark bei, einerseits durch direkte Verbesserung der Akquisition in örtlich beschränkten Regionen, andererseits durch ein generelles Verfahren zur Messung und Korrektur von Kodierungsabweichungen in diffusionsgewichteten Aufnahmen. Durch Weiterentwicklung und Kombination dieser Methoden mit anderen existierenden Verfahren bestehen weitreichende Möglichkeiten für zukünftige Verbesserung in vielen Bereichen der MR-Bildgebung und MR-Spektroskopie.

Chapter 1

Introduction

Magnetic Resonance Imaging (MRI) has proven to be a powerful technique for medical diagnoses of a wide variety of diseases. Among the various contrast mechanisms in MRI, diffusion-weighted imaging (DWI) [1, 2] and diffusion tensor imaging (DTI) [3] allow probing of random, Brownian motion of water protons on a per pixel basis. Generally, any interaction of the water molecules with cell membranes, intracellular structures or macromolecules will affect the extent of proton mobility (i.e. proton diffusivity), which can be assessed by means of these techniques. Quantitative values derived from DWI and DTI such as the mean apparent diffusivity or measures characterizing diffusion anisotropy can serve as markers for clinical diagnosis. These measures allow the investigation of processes that affect tissue integrity, as well as destruction and repair mechanisms, on a cellular level. In this context, diffusivity can be monitored over the time course of a disease, thereby providing a valuable tool to aid in the understanding of the underlying pathologic processes, and ultimately improve medical treatment.

Throughout the last 15 years, DWI techniques have evolved from the experimental research laboratory into clinical applications for the diagnosis of pathologies of the central nervous system, such as ischemia, tumors, trauma, and multiple sclerosis [3, 4, 5, 6]. Among the most common applications of DWI is the diagnosis of acute ischemic stroke where changes in proton self-diffusion reflect alterations on cellular homeostasis. Detection of these alterations using DWI is possible within hours after a stroke, thus directly impacting therapy decision and outcome. Furthermore, tumor infiltration on a cellular level can affect the integrity of neural tissue, leading to a decrease of diffusion anisotropy in areas that appear normal with conventional MR imaging techniques [8]. Similarly, changes in tissue diffusitivity, can help in the early detection of disruption and degeneration of white matter tracts following traumatic brain injury. In multiple sclerosis, DWI helps to identify occult lesions and diffuse changes in white matter integrity that are not visible in conventional anatomical contrasts. Although the detection of these diseases is of equal importance in both the brain and spinal cord, DWI of the spinal cord has yet to be incorporated into clinical practice due to the technical difficulties associated with the small cross-sectional area, pulsitile motion, and inhomogeneous magnetic environment. These technical difficulties, which will be discussed in greater detail in section 1.2, are the driving force for the development of new concepts in MR sequence design to achieve robust DWI of the spinal cord.

1.1 Measuring Diffusion with Magnetic Resonance

In an external magnetic field the phase ϕ of a spin at location r at a time point t after excitation is given as

$$\phi(t) = \gamma B_0 t + \gamma \int_0^t G(\tau) r(t) d\tau \tag{1.1}$$

where B_0 is the static magnetic induction field, G is a superimposed linear field gradient and γ denotes the gyromagnetic ratio. The spatially dependent phase terms caused by the application of G provides the basis for spatial encoding in many MR experiments.

The most common MR sequence to achieve strong diffusion weighting is the Stejskal-Tanner sequence [7]. In this spin echo experiment the sample is initially excited with a 90° radio frequency (RF) pulse and then refocused by a 180° pulse with identical diffusion sensitizing gradients on both sides of the refocusing pulse (Fig. 1.1). By Eq. (1.1) the phase of a spin at the echo time TE in this sequence is given as

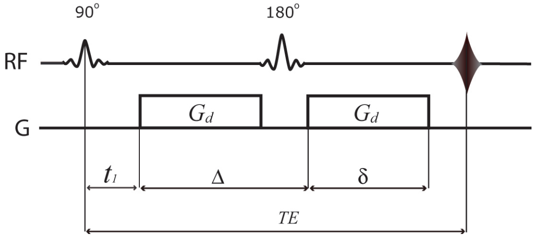

Figure 1.1: Diffusion-weighted spin echo experiment: diffusion sensitizing gradients of strength G_d, duration δ, and inter gradient delay Δ. The sample signal is acquired at the time TE when the spin echo is formed.

$$\phi(TE) = \gamma \int_{t_1}^{t1+\delta} G(\tau)r(\tau)d\tau - \gamma \int_{t_1+\Delta}^{t_1+\Delta+\delta} G(\tau)r(\tau)d\tau. \tag{1.2}$$

The phase effects induced by the diffusion gradients before the refocusing pulse are reverse by the second gradient lobe in the absence of motion. In a diffusive environment, each spin will accrue an individual phase depending on its random displacement path $r(\tau)$ along the diffusion gradient. Thus the magnetization M given as the vector sum of all magnetic moments therefore will ultimately be attenuated in the presence of diffusion. Assuming purely Gaussian diffusion processes the resulting signal can be calculated as [7]:

$$M(b) = M_0 e^{-bD}, \tag{1.3}$$

where M_0 is the reference magnetization measured in the sample without diffusion-weighted gradients, D is the diffusion coefficient [8] and b (commonly referred to as the b-factor) is the diffusion-weighting factor. In a Stejskal-Tanner experiment assuming rectangular gradient shapes, b can be calculated by the duration δ, amplitude G_d and the time shift Δ of the diffusion-sensitizing gradients:

$$b = \gamma^2 G_d^2 \delta^2 (\Delta - \frac{\delta}{3}) \tag{1.4}$$

By acquisition of two measurements using different diffusion-sensitizing factors b_0 and b_1, the diffusion coefficient can be calculated from the corresponding signal amplitudes using Eq. (1.3):

$$D = -\frac{ln(M(b_1)/M(b_0))}{b_1 - b_0}. \tag{1.5}$$

This concept can directly be extended to measure three-dimensional diffusion processes. In this case several experiments have to be performed with varying orientation of the diffusion gradients. In the most commonly employed method, diffusion is characterized by the so called diffusion tensor [9].

1.2 Imaging Artifacts

In the above section the basis of diffusion encoding and measurement was introduced. To obtain an image, spatial encoding on the image level is added, which is usually being described in the well established k-space picture [10]. The combination of both experiments (i.e. diffusion weighted imaging) is challenging in many respects. In the following a short summary of common MR imaging artifacts and their considerations in the context of DWI sequence design is given:

- *Low signal-to-noise-ratio (SNR)*: As discussed in the last section diffusion is quantified by the signal attenuation caused by the diffusion sensitizing gradients. Therefore DW images inherently suffer from low SNR. To achieve high image resolution within clinically feasible scan time, SNR efficient scanning techniques as well as acquisition at high field strength is highly desirable.

- *Motion artifacts (ghosting)*: For so called *multi-shot* imaging sequences such as interleaved echo planar imaging (EPI) or the conventional spin echo sequence the k-space is acquired in several segments. Due to physiological motion (cardiac pulsation, respiration), varying phase shifts are introduced to the segments that are measured in independent experiments. For non-diffusion weighted scans, the patient motion must be quite large to introduce a phase shift sufficient to cause so called *ghosting* artifacts. However, in the presence of the strong diffusion gradients even minor motion will lead to large phase shifts causing sever Ghosting artifacts.

Among diffusion weighted sequences spin echo EPI sequences probably achieve the highest SNR efficacy. A combination with a single-shot acquisition is highly desirable to avoid motion induced ghosting-artifacts. However, with single-shot imaging techniques the readout times are relatively long, as data for one image has to be acquired in a single acquisition. For such long readout trains several further problems have to be considered:

- *Susceptibility artifacts*: The static magnetic induction field B_0 is influenced by the magnetic susceptibility of the sample tissue. Especially at high field strength differences in magnetic susceptibility in the sample will lead to a local variation $\delta B_0(r)$ of the magnetic induction. As being apparent from Eq. (1.1) deviations from the nominal field strength will cause phase terms accumulating over time. Therefore imaging sequences with long readout durations commonly suffer from artifacts related to unaccounted phase effects. The induced local distortions are particularly problematic for imaging in regions with nearby bone structures or at air-tissue interfaces.

- *Image blurring*: In MRI signal intensity during the readout decays exponentially characterized by the tissue specific time constant T_2^*, which decreases with higher field strength. This signal decay causes a weighting of the acquired signal, which depending on the chosen sampling strategy (i.e. the k-space trajectory) causes a weighting of the k-space data. In case of a single-shot EPI readout the imposed signal weighting results in broadening of the so called point-spread function (PSF) and therefore leads to image blurring, ultimately limiting the achievable image resolution.

- *Eddy-currents distortions*: When a magnetic field gradient is applied, the change in magnetic flux density, dB/dt, induces an eddy current which according to Lenz's law in turn creates an extra magnetic field. Due to the complex geometry of the scanner system eddy current induced fields are difficult to predict. As compared to anatomical MR sequences, the increased gradient amplitudes in DWI and fast slew rates of the DW gradients induce drastically increased eddy current effects, which, if not accounted for, can result in image distortions. This is problematic since variably diffusion encoded data must be perfectly congruent to permit fitting diffusion data to models such as the diffusion tensor. Moreover, these fields are suspected to have considerable components being non-linear in space, which further complicates their prediction and correction.

1.3 Objectives and Outline

The aim of the present dissertation is to improve the acquisition of DWI and DTI at high field strength (3T). The specific goals are to develop acquisition techniques and reconstruction mechanisms that allow high-resolution DWI and DTI of the spinal cord. To achieve insensitivity against artifacts induced by the strong pulsatile motion of the cerebrospinal fluid around the spinal cord and the spinal cord itself, the use of single-shot techniques is essential. Robustness against artifacts caused by the increased susceptibility differences in this region of the body as well as image blurring is accomplished by a reduced field-of-view (FOV) approach which permits a drastic reduction in readout duration for a given image resolution. FOV reduction is achieved by outer volume suppression which is described in chapter 2, enabling robust acquisition of at the cervical level of the spinal cord. In chapter 3 this technique is extended to enable DW imaging in the entire spinal cord, by combining outer volume suppression with an oblique spin-echo selection.

The problem of eddy current induced by the strong diffusion weighted gradients is approached on a general level by the development and application of magnetic field monitoring. In magnetic field monitoring NMR field probes are employed to measure the actual field evolution during an MRI readout. Thereby allowing to deliberately tolerate eddy-current induced field deviations from the nominally applied dynamic field evolution and account for them during image reconstruction. Allowing simultaneous acquisition of field probes and imaging data requires excitation of both, the imaging object and the field probes prior to the readout. In the early days of field monitoring this was performed using the scanners RF system by first separately exciting each field probe and then the imaging object, which imposes constraints on the sequence design as well as accepting signal loss from the NMR probes. In particular this method was not feasible for diffusion weighted acquisition, as the strong diffusion sensitizing gradients would cause complete dephasing of the probes signal. A solution was found in the development of a transmit/receive system using shielded NMR probes which is described in chapter 4. The separate transmit/receive chain allows excitation of all field probes simultaneously after the second diffusion sensitizing gradient just before their readout. Furthermore the shielding of the field probes makes them immune to RF from the scanner system thereby avoiding unwanted excitation and signal

loss.
In the last chapter, this approach is applied to solve the problem of eddy-current induced distortions in DWI. In order to do so a field camera was constructed using 16 NMR field probes. With this field camera not only linear field contributions, but also higher-order dynamic field evolution can be assessed. In particular all field contributions including the higher-order field terms induced by the DW gradients can be measured. Finally a reconstruction algorithm that is capable of incorporating and correcting higher-order fields is described in chapter 5.

Chapter 2

Outer Volume Suppression for Cervical Spinal Cord Diffusion Imaging

2.1 Introduction

In recent years diffusion tensor imaging (DTI) [9] in the brain has become feasible for the investigation of various neurological pathologies affecting the human brain. In the spinal cord however, this method still has not found its way into clinical applications, although it is expected to improve our understanding on the nature and evolution of structural damage in several clinical situations such as inflammatory demyelination, spinal cord infarction, amyotrophic lateral sclerosis, Wallerian degeneration, compressive myelopathy, and spinal cord mass lesions.

In the brain the most established approach for acquiring diffusion weighted (DW) images is single shot echo-planar-imaging (SS-EPI). This technique benefits from an inherent robustness against ghosting artifacts from physiological motion and from a relatively high signal to noise ratio (SNR), which can be further improved by acquisition at higher field strength (3T). In the spinal cord, SS-EPI suffers from strong susceptibility gradients induced by the surrounding tissues, particularly the osseous elements of the spinal column. This problem increases at 3 T, and the readout train for a conventional SS-EPI acquisition with sufficient resolution to image the spinal cord will be too long to give images of adequate quality.

To reduce the readout duration several approaches have been used. At 1.5 T, parallel imaging (PI) has been successfully applied to reduce the readout duration for spinal cord diffusion imaging [11, 12]. At 3 T however, there are currently no suitable coils available for the cervical spinal cord to allow high PI reduction factors, thus limiting the achievable spatial resolution. Multi-shot imaging, where k-space is split into several acquisitions with multiple interleaves is possible, but complicated by the complexity of physiological motion (particularly CSF pulsations). This technique has commonly been used for EPI readouts [13]. Other non-EPI approaches such as Turbo Spin Echo (TSE) [14, 15] and linescan [16] have been successfully tested for spinal cord diffusion weighted imaging (DWI). These are more robust against susceptibility distortions and chemical shift artifacts, but they suffer from low SNR or prolonged scan time. The morphology of the spinal cord, particularly its small cross-sectional dimensions, makes it possible to use a reduced FOV approach, with a rectangular FOV centered on the region of interest. The corresponding reduction of the required number of k-space lines enables single-shot EPI with shorter readout duration, leading to a reduction of susceptibility artifacts. However, to prevent aliasing artifacts, the acquisition of signal from the region outside the FOV, i.e. the outer volume (OV) has to be avoided. Reduced FOV approaches for spinal DWI in the transverse plane have been proposed [17] (ZOOM-EPI) using a tilting of the echo pulse to the excitation pulse thus creating a spin echo localized only at the intersection of the two pulses. The rhomboid shape of the spin echo profile prevents a full FOV reduction in phase direction, requiring slight k-space over-sampling and the acquisition in several packages may prolong the overall scan time. Another approach for spinal DWI in the sagittal plane is using a localized spin echo by applying the echo pulse in the phase direction and a second 180° pulse after the EPI readout to reduce the loss of SNR for multislice acquisition [18]. For the approach presented here, aliasing in the reduced FOV was avoided by suppressing the OV with specifically designed presaturation slabs. The aim of this paper was to develop a technique for DWI of the cervical spinal cord in the transversal plane insensitive to susceptibility and motion artifacts within clinically relevant scan times. The technique should be capable of producing images within clinically relevant scan times for DTI acquisitions. A single-shot EPI approach using a reduced FOV to shorten the readout train length and thereby minimize susceptibility distortions is suggested. An outer volume suppression (OVS) sequence [19] using quadratic phase pulses [20] is optimized for its application in the cervical spinal cord. Additionally, a spin echo fat suppression by gradient reversal technique [21] is implemented to avoid water fat-shift artifacts. The performance of the suggested technique was evaluated by in-vitro and in-vivo scans.

2.2 Theory

2.2.1 Outer Volume Suppression

OVS utilizes one or more spatially selective pulses, applied in the OV regions followed by dephasing gradients. The OVS sequence is placed before the slice excitation pulse of the imaging sequence. Effective OVS requires complete dephasing of the transverse magnetization and nulling of all longitudinal magnetization at the time of the excitation pulse. In the present case the regions on both sides of the spinal cord have to be suppressed. Hence, separate OVS pulses must be applied on the left and right side of the FOV in phase direction. In absence of transversal magnetization, the longitudinal magnetization at a time i after the ith pulse in a pulse train may be calculated according to:

$$M_i = M_i e^{-(\tau_i/T_1)} cos(\alpha_i) + M_0 - (\tau_i/T_1). \tag{2.1}$$

Here M_{i-1} is the longitudinal magnetization just before application of the i'th pulse, α_i is the flip angle of the i'th pulse, and M_0 is the equilibrium magnetization. The design of a sequence that accomplishes effective OVS requires optimization of several parameters. First, the pulse type has to be chosen: The presaturation slabs should be highly selective broad-banded pulses in order to excite a well defined spatially broad region (here 60 mm) even in regions of inhomogeneous B0. For this reason quadratic-phase Shinnar-Le-Roux (SLR) pulses as designed by Schulte et al. [22] were used. The pulses frequency sweep causes a consecutive flipping that traverses the bandwidth (BW) from start to stop band over the time of application similar to adiabatic pulses [23]. For our purpose the fractional transition width (FTW) defined by transition width (TW) / BW was fixed

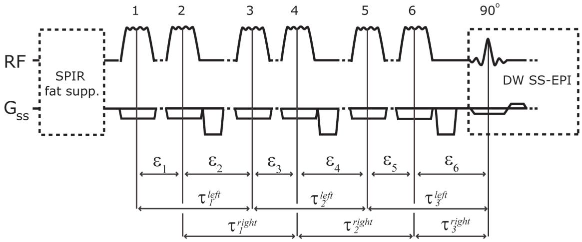

Figure 2.1: Schematic representation of the DW SS-EPI sequence preceeded by the presaturation OVS sequence and the SPIR pulse. Each pair of quadratic-phase pulses (first pulse for left and second for the right slab) is followed by crusher gradients. ϵ_i denotes the interval between the center of the i'th and the center of the following pulse while τ_i is the time between two consecutive pulses applied in the same geometric region. G_{ss} denotes the gradient in slice selection direction.

such that the transition band had a spatial width of 4 mm, while all pulses had a minimum BW of 4700 Hz, thus fixing the pulse durations dur_i for each flip angle α.

Multiple application of suppression pulses offers the possibility to enhance T_1 insensitivity and/or B_1 insensitivity of the OVS. For each saturation region (left and right) three pulses were used, still allowing acquisition of one slice per cardiac cycle without violating specific absorption rate (SAR) limitations. To keep the OVS applicable for arbitrary interacquisition delays (that may change by the number of slices acquired each TR, or by changing cardiac frequencies for cardiac triggered acquisitions) the first two flip angles for each slab were fixed to 90°. This achieves a B1 insensitive nulling of the longitudinal magnetization of all OV tissue in the first part of the OVS sequence independently of their (initial) longitudinal magnetization before the OVS sequence. The 6 pulses were fixed to affect left and right outer volume in an alternating manner, to minimize the number of required crusher gradients (figure 2.1). The interpulse timings ϵ were fixed to the shortest practical value (while still nulling longitudinal magnetization at excitation time) to improve T_1 insensitivity and decrease the total time of the OVS sequence. A schematic representation of the presaturation pulse sequence is given in figure 2.1.

2.2.2 Fat Suppression

Fat suppression is usually implemented by a spectral inversion recovery (SPIR) pulse preceding the slice selection pulse, creating the need to place the SPIR pulse before the OVS. Due to the application of the OVS pulses, the fat suppression in the transition bands of the pulses turns out to be unsatisfying, thus, resulting in fat-shift artifacts. Therefore, additionally to the SPIR pulse preceding the OVS, a reverse gradient technique was implemented [21, 24]. With this technique the slice selection gradient and the echo gradients are assigned opposite signs. The technique utilizes the high water-fat-shift and the small BW of the slice excitation and echo pulse in the spin echo sequence. In the current implementation, an excitation pulse BW of 533 Hz and an echo pulse BW of 572 Hz is used, while the fat band shifts -440 Hz for the excitation and +440 Hz for the echo pulse as compared to the center (water) frequency. This leads to a complete spatial disjunction of the fat compartments, which are subject to excitation and echo pulse respectively, thus avoiding echo generation from fat protons. In order to unwanted signal rephrasing, all gradients on the slice selection axis preceding the excitation pulse were assigned the same sign as the slice selection gradient (figure 2.1).

2.3 Materials and Methods

2.3.1 OVS optimization

Numerical optimization of the OVS for the free parameters, i.e. the 3rd flip angle α_3, and the interpulse durations ϵ_i (see figure 2.1) was performed on a personal computer using matlab 7.0.1 (The MathWorks, Inc., Natick, MA). The simulation minimized longitudinal magnetization at the time of the excitation pulse for tissues having a T_1 of 292 ms, and 1160 ms (approximate relaxation times at 3 T for fat and skeletal muscle) for the left and right OV respectively. Pulse intervals ϵ_i were constrained by the pulse durations and by the time required for dephasing gradients and eddy-currents-decay-periods. For the optimized parameter configuration residual longitudinal magnetizations were calculated for a range of T_1 (280-1500ms), which covers the range of in vivo tissue. To account for the frequency sweep of the quadratic-phase pulses, timing offsets of up to ± dur/2 of the pulses nominal application time were incorporated into the calculations, as well as flip angle variations due to B_1 inhomogeneities of -20 % to +5 %, according to [25] for the in-vivo variation of the B_1 field. The sequence resulting in a minimal maximum residual longitudinal magnetization over the whole range of T_1 was chosen as optimal.

2.3.2 MR Scanning

All imaging was performed on a 3T Philips Achieva MR system (Philips Medical Systems, Best, The Netherlands) using a 12 element phased array spine coil.

In Vitro Scans

The optimized OVS sequence obtained with the numerical simulation was tested in-vitro and was evaluated for its efficacy of suppression and for effects that had been neglected by the simulations, like excitation profiles and the generation of unwanted stimulated echoes. To simulate in vivo behavior of skeletal muscle and fat tissue in a phantom, liquids with corresponding T_1 relaxation constants (distilled water doped with Gadolinium to T_1 1160 ms, and vegetable oil with T_1 290 ms) were filled into a bottle. To evaluate residual signal from the suppressed areas, the phantom was scanned on a full FOV with a T_2 weighted multi-shot EPI sequence to avoid susceptibility artifacts while acknowledging the potential occurrence of EPI-ghosting artifacts. The full FOV covered the entire phantom in the axial plane with the two suppression slabs (slab width 60 mm each) applied on the left and right part of the image while leaving the middle portion of the image unsuppressed. Scan parameters were FOV = 130 × 130 mm2, matrix = 144 × 144, TR = 3000 ms, TE = 40 ms, slice thickness = 5 mm and signal averages = 10. An EPI-factor of 15 was used to avoid susceptibly effects and to create a clearly visible fat-shift of 11.4 pixels in the anterior direction to separate lipid and non-lipid spins in the oil compartment of the phantom. To evaluate residual signal in the different liquid compartments, two sets of images were acquired, one using OVS and fat suppression, and one without. The efficacy of the suppression, defined as the fraction of suppressed to unsuppressed signal, was measured in different regions of interest (ROIs) placed in each of these image pairs. To illustrate the effect of the different methods combined in this approach, images with OVS but without fat suppression and images with OVS and SPIR fat suppression only were acquired additionally.

In Vivo Verification

In-vivo, 2D - spin-echo, SS-EPI DTI data of the cervical spinal cord were acquired between levels C-3 and C-5 in 5 healthy subjects. Images were acquired in axial orientation using the optimized OVS sequence. Acquisition (slice thickness = 5 mm, NEX = 6 / 12 for b = 0 / b = 750 s/mm2, matrix = 144 × 36, FOV = 130 × 32.5 mm2, TR = 3500 ms, TE = 40.6 ms) was carried out along six diffusion directions $(-2/3, -1/3, -2/3)^T$, $(1/3, 2/3, -2/3)^T$, $(-2/3, 2/3, 1/3)^T$, $2^{-1/2} \cdot (1, 1, 0)^T$, $2^{-1/2} \cdot (0, -1, -1)^T$, $2^{-1/2} \cdot (1, 0, -1)^T$ with a b-factor of $750 s/mm^2$. Additionally, for each slice a baseline image with minimal diffusion weighting (b_0-image) was acquired. The shortest possible readout train duration (i.e. highest readout BW) was chosen and further shortened by a partial Fourier encoding of 0.6 to limit T_2^* decay and phase effects from susceptibility gradients. The phase encoding direction was set left-right (LR) to avoid high signal foldover originating from tissue near the coil surface. The reduced number of phase encoding lines resulted in reduction of EPI-readout time from 111 ms to 28 ms as compared to a full FOV Matrix size of 144 × 144. Scan time was 48 s per slice for a multislice setup due to SAR restrictions.

2.3.3 In-Vivo Processing and Visualization

Retrospective interscan motion correction for in-vivo data was performed using a 3D-rigid co-registration algorithm[26]. Subsequently, eddy current-induced image warping was reduced with a correlation-based 2D-affine registration algorithm[26]. An isotropically DW image was calculated as the geometric mean of three orthogonal DW images served as a reference for the registration process, since these images show high contrast between spinal cord (and nerve roots) and CSF. The six DW images and the b_0-images were registered to this reference. From these datasets, the mean apparent diffusion coefficient (ADC), relative anisotropy (RA) and fractional anisotropy (FA) [27] were calculated. ROI's covering GM and WM respectively were carefully placed in each slice after close considerations of the anisotropy, DW, and T_2 weighted images.

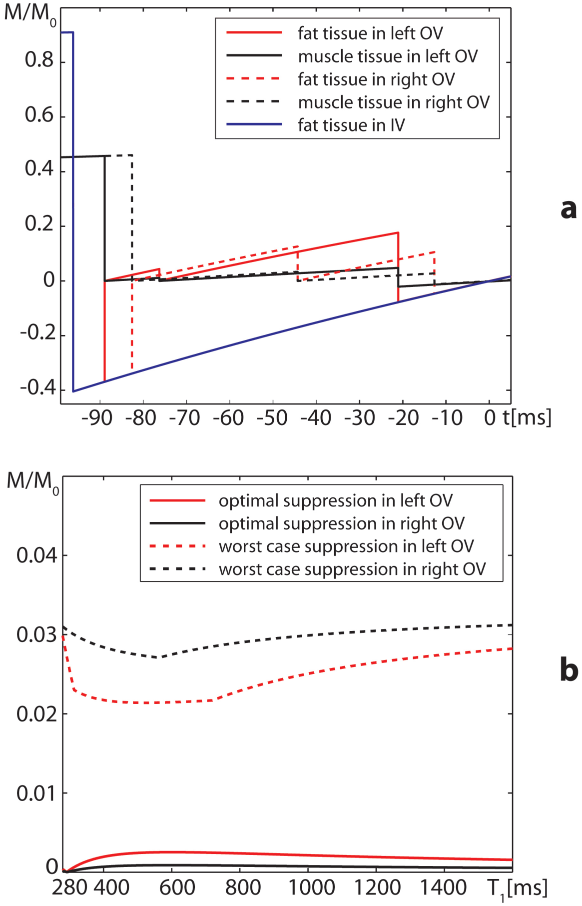

Figure 2.2: Simulated longitudinal magnetization in the different tissue compartments over the time course of the application of the optimized OVS sequence neglecting T_1 and timing offsets. (b) Residual longitudinal magnetization M/M_0 in the left and right outer volume versus T_1 for the optimized OVS simulated without (optimal) and with (worst case) the effect of maximal B_1 variations and timing offsets.

i	1	2	3	4	5	6
ϵ_i	6.5 ms	8.6 ms	33.1 ms	24.0 ms	8.7 ms	13.23 ms
α_i	90	90	90	90	116	116
dur_i	6.5 ms	6.5 ms	6.5 ms	6.5 ms	8.7 ms	8.7 ms

Table 2.1: The optimized configuration for the OVS sequence.

ROI	FA (μ, σ)	RA (μ, σ)	Mean ADC $(\mu, \sigma)[10^{-3}mm^2/s]$
GM	0.56 ± 0.14	0.53 ± 0.15	0.94 ± 0.14
WM	0.76 ± 0.10	0.81 ± 0.15	0.97 ± 0.15

Table 2.2: Measured quantitative diffusitivity values averaged over all 5 subjects (ROI sizes: GM = 80 voxel / subject; WM = 170 voxel / subject).

2.4 Results

2.4.1 Simulation

For each maximum flip angle α, the numerical optimization returned the inter pulse timings ϵ to achieve a theoretical nulling of the longitudinal magnetizations M_z in all compartments at excitation time, which is displayed for the finally chosen parameter constellation in figure 2.2(a). When taking timing variations due to the frequency sweep and flip angle variations into account, an optimum, defined by a minimal maximum error of residual fat and water signal, was found for a flip angle of 116°. The parameters of this optimized OVS sequence are given in table 2.1. Even when assuming maximum flip angle variations and timing offsets (named ”worst case suppression”in figure 2.2(b)), the residual longitudinal magnetization was no more than approximately 3 % for the whole range of tissue T_1.The theoretical minimum did not exceed 0.25 % (figure 2.2(b)). The difference in efficacy of the suppression in left and right OV results from timing differences of the OVS pulses.

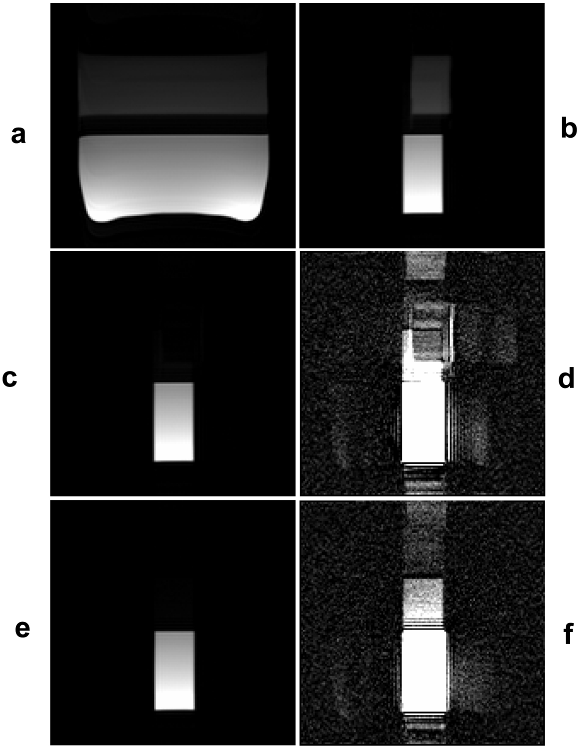

Figure 2.3: MS-EPI images of a phantom with water (below) and oil (above) with its lipid section shifting to anterior. (a): Without OVS or fat suppression. (b): with OVS but without fat suppression, (c,d): with OVS and SPIR fat suppression and (e,f): with OVS, SPIR fat suppression and gradient reversal fat suppression. (d) and (f) showing the same data as (c) and (e) respectively with the window set to display noise level. (d) displays the residual inner volume fat shifting to above (anterior) - left (readout and slab selection fat-shift) with hyperintense signal in the TW of the suppression pulses. (f) shows complete suppression of all lipid signal; only inner volume water-spins exhibit signal.

2.4.2 In-Vitro Scans

Figure 2.3 demonstrates the effect of the different modules of the sequence on the suppression profiles. The residual signal, measured in the different ROIs (table 2.2) from repeated multi-shot EPI measurements (figure 2.3(a,e)), was approximately 1 % in the "muscular"compartments (T_1=1160 ms). For the inner and outer volume lipid compartments the residual signal was below the noise level (not measurable) despite their high SNR in the unsuppressed images (table 2). Suppression profiles were well defined, and no artifacts from spurious echoes were visible in any acquired dataset (figure 2.3(b-f)).

2.4.3 In Vivo Scans

Figure 2.4 a shows the obtained images in the contrasts T_2, mean DW, mean ADC and RA. To appreciate the robustness of our method, the center image of the imaging stack for each subject is shown in the mean DW and RA contrast (figure 2.4). No susceptibility artifacts, motion artifacts or water-fat shift artifacts due to insufficient inner volume fat suppression were observed in any of the acquired datasets. Fold-over artifacts, indicated by structured hyper or hypo intensities not in accordance with anatomical structures, were absent on both DW and T_2W images. Particularly, the hypointense CSF in the DW images did not show any local hyperintensities in any of the acquired slices (figure 2.4). The GM was depicted slightly hyperintense compared to the WM on T_2W and mean DW images. GM-WM contrast was better displayed in the anisotropy images, with the white matter appearing hyperintense due to its high content in myelinated fibers. However, not all anisotropy images showed the expected butterfly-shaped GM, which is also reflected in the relatively high standard deviations of the mean calculated diffusivity values (Table 3). Nerve roots were best visible on the mean DW images (figure 2.4(a,b)), but only faintly visible in all other contrasts.

2.5 Discussion

We have introduced a reduced FOV approach for spinal cord diffusion imaging in the transverse plane at 3T. The resulting reduction of the required number of k-space lines made high resolution SS-EPI acquisition

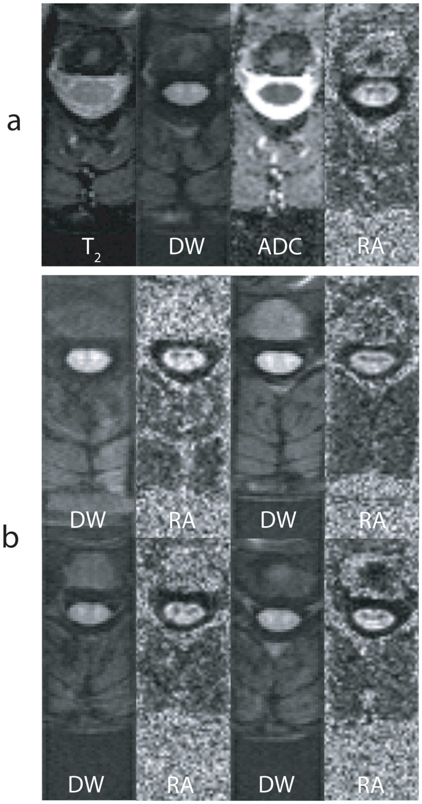

Figure 2.4: Transversal slice of the spinal cord at level C4 (center slice of imaging stack) in different contrasts. (a): Subject 1: T_2, mean DW, mean ADC, and RA. (b): Subject 2-5: mean DW and RA.

possible without the occurrence of susceptibility artifacts. The good image quality is accredited to the TE shortening and thereby reduced T_2 decay, as well as to the shorter readout leading to reduced T_2^* blurring. Being a single shot acquisition technique, imaging was also robust against ghosting artifacts from physiological motion. Fold-over artifacts were efficiently avoided by optimization of OVS and fat suppression techniques. Simulations showed a maximum residual signal of approximately 3 % when assuming worst-case timing offsets (due to the pulses frequency sweep) and B_1 variations as expected in-vivo for the optimized OVS sequence. In-vitro evaluation of the optimized OVS showed a mean residual signal from the OV of less than 1 % with reasonably low standard deviation. The gradient reverse fat suppression technique proved efficient in avoiding spin echoes from lipid compartments without the cost of extra RF deposit. Depending on the required bandwidths of the spin-echo pulses, this T_1 insensitive fat suppression technique may be employed in the future without the SPIR even on 3T. Due to the high bandwidth of the quadratic phased pulses, the OVS sequence performed well even in areas with problematic shimming. The influence of the in-vivo B_1 variation may also differ as compared to the in-vitro setup, but is generally considered to be smaller than in the phantom. Thus, OVS and fat suppression are expected to be even more stable when applied in-vivo. This was confirmed by the in-vivo results, where no artifacts related to fold-over effects or water-fat-shift were visible in any DW or T_2W images. The fact that the anisotropy contrast did not display the expected butterfly-shape of the GM consistently in all images may be attributed to the relatively low SNR, partial volume effects and possibly also to imprecise coregistration. It may also be for these reasons, that the measured FA values were higher than the previously reported values of FA(WM) = 0.65, FA(GM) = 0.34 [16], and the contrast in mean ADC was less discriminative than mentioned in [28] (mean ADC(WM) = 0.77 - 0.80; mean ADC(GM) = $1.0 - 1.110 - 3mm^2/s$. To the authors knowledge these are the only published data distinguishing the diffusitivty values of GM and WM. The in-plane resolution of 0.9 mm × 1.05 mm for axial DWI of the spinal cord, was similar to other studies 1.25 mm × 1.25 mm [16, 17], and 0.96 mm [29]. In this work the data was acquired without cardiac triggering, but the technique may readily be combined with cardiac triggering when for example acquiring data for fiber tracking, or for more accurate measurement of diffusivity values. This will only minimally prolong the scan time, and has also been tested with promising results. The presented methods were integrated into the software of our clinical MR system. Hence, OVS and the reverse fat suppression technique can be combined with the existing sequences via the user interface without further modifications or preparations. In comparison to parallel imaging, this approach is naturally immune to sensitivity miscalibration. Furthermore, for the same reduction of sampled k-space lines, the images produced by parallel imaging will have a lower SNR by a factor of 1/g, g being the coils geometry factor [30]. As compared to ZOOM-EPI [17], our approach provides a more effective readout time reduction due to the well defined rectangular signal profile. Furthermore, multislice acquisition does not require splitting the slice stack in multiple packages, which depending on the used geometry may prolong the scan time. In comparison to the reduced FOV approach [18] multislice imaging with our method will not result in signal loss. However, acquisition speed of our method is limited by SAR constraints to one slice acquisition every 750 ms. Both of the two mentioned reduced FOV approaches are limited to spin echo acquisitions, while this approach may also be combined with gradient echo techniques for other applications. The application of this technique in other regions of the spinal cord is desirable, but is currently limited by BW and residual OV signal from multiple fold-over.

2.6 Conclusions

We introduced OVS for reduced FOV SS-EPI spinal cord diffusion imaging in axial orientation. Reducing the FOV enabled high-resolution acquisition of the cervical spinal cord without visible susceptibility or motion artifacts. Water-fat-shift artifacts were successfully avoided by SPIR together with a spin echo gradient reversal technique. The virtually artifact free images and the short imaging time make this method promising for clinical application of diffusion imaging in the human cervical spinal cord.

Chapter 3

Diffusion Weighted Imaging of the Entire Spinal Cord

3.1 Introduction

Diffusion tensor imaging (DTI) [9] and diffusion-weighted imaging (DWI) are of significant clinical interest as means of non-invasively providing information about structural integrity of and alteration to neural tissue. Spinal cord trauma is the most common cause of acute paraplegia or quadriplegia, and alterations in axonal integrity may be relevant both for early injury diagnosis, predicting outcome and for monitoring treatment effectiveness and recovery. Further, investigations of diffusion characteristics in the spinal cord may reveal new clinical insights into pathologies such as inflammatory demyelination, spinal cord infarction, amyotrophic lateral sclerosis, Wallerian degeneration, compressive myelopathy, and spinal cord mass lesions [31].

Precise localization of focal pathologies in the spinal cord requires accurate depiction of its intrinsic anatomical structure - in particular differentiation of grey matter (GM) from white matter (WM). This is best accomplished by imaging the spinal cord in the transverse plane with small in-plane voxel sizes. The attainable resolution however is inherently limited by the achievable signal to noise ratio (SNR), driving interest in acquiring data at higher field strengths (3T) while maximizing SNR efficiency. Furthermore physiological motion and substantial susceptibility effects may compromise image quality in the spine depending on the readout technique that is used. Single-shot echo planar imaging (SS-EPI) techniques benefit from motion robustness and SNR efficiency, however, static field B_0 inhomogeneities originating from tissue susceptibility differences - that increase linearly with field strength - cause phase errors to accumulate during the long echo-planar readout trains leading to image distortion. Alternative readout techniques such as Turbo Spin Echo (TSE) [14, 15, 32], line scan 6 and stimulated echo acquisition mode (STEAM) [33, 34] are insensitive to such off-resonance effects, but suffer from lower SNR efficiency. To benefit from the SNR gain at higher fields, EPI acquisition with shortened readout duration is desirable. Segmented EPI, where k-space acquisition is split into multiple interleaving readouts is possible [15, 35, 13, 36], but impaired by the complexity of physiological motion. Parallel imaging has been applied to reduce the readout duration for spinal DW-SS-EPI [11, 12] at 1.5 T. However, in more caudal regions of the spine patient geometry restricts coil design so that parallel imaging is not effective in obtaining sub-millimeter in-plane resolution with adequate image quality. Recently, spatially reduced field-of-view (rFOV) SS-EPI approaches have shown promise for diffusion imaging of regions limited in at least one dimension. These have been implemented using either non-coplanar spin-echo (SE) selection [37, 38, 18], 2D-selective pulses [39, 40], outer volume suppression (OVS) [41] or combinations of these techniques [42]: For SE sequences a non-coplanar application of slice selective $\pi/2$ (excitation) and the π (refocusing) pulse allows a reduction of the FOV to the intersecting compartment of the slices where a spin echo is formed in tissue affected by both pulses (i.e. the SE selection domain). This technique was introduced by Feinberg et al. [37] who applied the excitation pulse with its slice selection gradient in phase encoding direction. However, for multiple-slice acquisitions this technique would lead to signal loss and strong T_1 weighting due to the saturating effect of the excitation pulse on neighboring material in the slice selection direction defined by the refocusing pulse. Jeong et al. proposed a similar approach [18] with the π pulse being selective in the phase encoding direction and a second π pulse after the EPI readout, thus reducing signal loss by restoring some of the longitudinal magnetization for the acquisition of other slices. Wheeler-

Kingshott et al. [38] proposed a method wherein the concept of line scan [16] was combined with an EPI readout. Here the π refocusing pulse is applied slightly oblique with respect to the imaging plane defined by the $\pi/2$ pulse (oblique SE selection), thereby achieving a FOV reduction to a rhomboidal region (having broadened transitions in the phase direction). The technique was recently modified [42] to incorporate a 2D-selective excitation pulse similar as proposed in [43, 40], which reduces the transitions in the excitation profile. However, as compared to 1D-selective pulses the quality of a 2D-selective excitation profile is highly sensitive to miscalibration of the gradient and RF system [44] while requiring prolonged pulse durations. An OVS sequence using quadratic phase Shinnar-Le Roux pulses [22, 20] recently was proposed to suppress the outer volume (OV) on both sides of the spinal cord [41]. This technique, achieving full SNR and highly selective inner volume (IV) selection, was optimized for efficient suppression even in the presence of in-vivo B_0, RF-field (B_1) and T_1 variations. However, technical constraints limit the application of this technique to regions such as the cervical spine where only a narrow OV region (¡ 6 cm) has to be suppressed. In the thoracic and lumbar spine the OV on left and right side of the spinal cord spans up to 20 cm, posing excessive demands in terms of bandwidth and fractional transition width of the OVS pulses. As bandwidth is proportional to the specific absorption rate (SAR), a similar robustness against B_0 inhomogeneity would yield a more than three fold increase of scan time for the same number of slices. Furthermore the pulse durations needed to fulfill bandwidths and transition widths requirements would cause a noticeable degradation of the suppression properties, leading to more residual signal from the OV that is additionally vastly extended. For the work presented here, we utilize the recent developments in OVS [41] in combination with oblique SE selection [38]. As compared to the rFOV techniques mentioned above, the approach benefits from achieving robust and effective FOV reduction such that it is applicable in the entire spinal cord. The high SNR efficiency allows for high-field diffusion imaging with improved in-plane resolution. Results in phantoms and healthy subjects are presented.

3.2 Materials and Methods

The proposed method is shown schematically in Fig. 3.1. Non-coplanar application of the $\pi/2$ and π pulse aims to reduce the SE selection domain

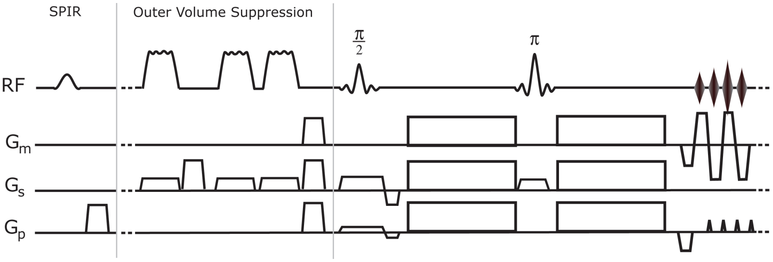

Figure 3.1: Schematic representation of the proposed sequences showing RF and gradients in measurement, slice and phase direction (G_m, G_s, G_p). The SPIR fat saturation pulse precedes the OVS sequence. Crushers in all direction prevent the occurrence of spurious echoes generated during SPIR and OVS sequence. Tilting of the $\pi/2$ pulse is achieved by an additional gradient in phase encoding direction during the $\pi/2$ slice selection.

in phase encoding direction in order to reduce the FOV along this dimension without incurring aliasing artifacts. Perpendicular application of the $\pi/2$ (or π) pulse would lead to the desirable rectangular profile (Fig. 3.2a), but would at the same time lead to an excitation of all other slices and thus would give low signal when used in a time efficient multiple-slice setup. For this reason the excitation plane is slightly tilted (Fig. 3.2b) with respect to the imaging plane such that this effect impacts neighboring slices only, thus enabling multiple-slice imaging if scanning in a dedicated interleaved slice order. However, only the fully refocused center part of the rhomboidal SE selection domain can be used for imaging. To eliminate the unwanted transitions in this SE selection domain, OVS is additionally applied on both sides of the FOV (Fig. 3.2c). Figure 3.1 shows the proposed diffusion weighted SS-EPI sequence with the OVS sequence preceding the SE excitation pulse and the additional gradient in phase encoding direction implementing the tilting of the π excitation plane.

3.3 Oblique SE selection

Throughout this paper, the term package refers to a set of spatially separated slices imaged within one repetition time (TR) to avoid slice cross-talk. With the aim of having no slice gap in the imaging stack, the max-

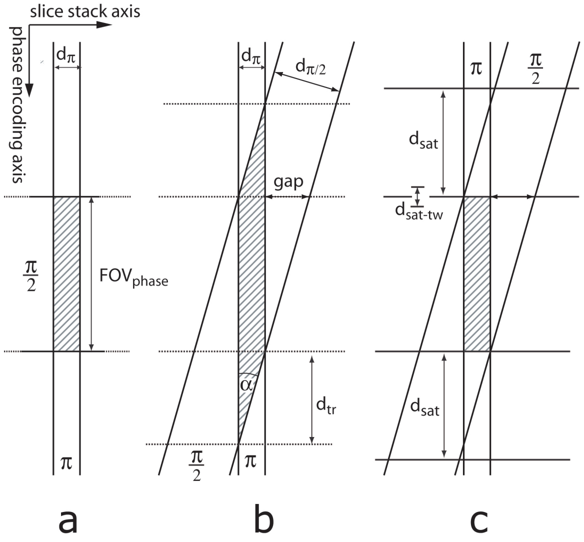

Figure 3.2: Schematic geometries of different approaches to defining a signal profile limited in the phase direction. (a): The $\pi/2$ pulse is applied perpendicular to the imaging plane, thus affecting all slices in the imaging stack. (b): The $\pi/2$ pulse is applied tilted by a small angle α with respect to the imaging plane. The approach allows multiple-slice acquisitions, but achieves an imperfect signal profile with an unwanted transition width dtr. (c): The $\pi/2$ is again tilted by an angle α, but additional OVS slabs (slab width $d_{sat} \geq d_{tr}$) are applied on both sides. The profile's transition width is now given by the transition width of the OVS pulses d_{sat_tr}.

imum tilt angle α for which excitation of slices belonging to the same imaging stack is avoided for a given maximum number of packages p, may be calculated as

$$\alpha = arctan\left(\frac{(p-1)z}{FOV_{phase}}\right), \tag{3.1}$$

where the slice thickness z is given by the width of the refocusing pulse d_{π} and FOV_{phase} is the size of the FOV in phase direction (Fig. 3.2). The transition width of the SE selection domain d_{tr} can be calculated by:

$$d_{tr} = \frac{z}{tan(\alpha)} = \frac{FOV_{phase}}{p-1}. \tag{3.2}$$

In order to achieve time-efficient scanning even for a small number of slices, we restrict the number of packages to two. Given the above equations, a FOV_{phase} of 30 mm and the slice thickness $z = 2.5$ mm (5 mm) yield α to be 4.76° (9.46°).

As the $\pi/2$ pulse is applied in a non-coplanar manner with respect to the imaging plane, the image signal intensity in phase direction will be weighted by the pulses' excitation profile. To achieve a homogeneous profile within the FOV, and in order to avoid slice cross-talk, the use of a virtually rectangular signal profile of the excitation pulse is desirable. This was achieved by the use of a sinc waveform with Gaussian apodization (time bandwidth product = 90.71, pulse duration = 3.65 ms).

3.4 OVS

To suppress signal from the transition bands of the SE selection domain (Fig. 3.2b), OVS similar to our previous work [41] is applied with timings and flip angles optimized for the range of in-vivo tissue T_1 and B_1 variations. This OVS scheme has been shown to suppress OV contamination to around 1% in phantom experiments, a result which has been confirmed by in-vivo experiments showing no visible aliasing artifacts. Fat suppression is implemented as a spectral inversion recovery (SPIR) pulse preceding the OVS sequence (Fig. 3.1). In this fashion, lipid signal is suppressed efficiently in the IV and OV. However, in the transition bands of the OVS slabs, pulse shape and bandwidth variations may cause fat tissue being unaffected by some OVS pulses, resulting in incomplete fat suppression in these areas. To avoid shifting of this residual lipid signal into the center of the FOV, the effective EPI fat-shift in phase encoding direction and fat-shift at OV selection are set to sum up to a multiple of the FOVphase size. This is achieved by slightly reducing the OVS suppression pulses bandwidths, while acknowledging slight impairment of the suppression characteristics. As a positive side-effect, lower specific absorption rate (SAR) allows the acquisition speed to be increased, permitting one acquisition in each cardiac cycle for heart rates ≤ 88 beats / minute. All inter-pulse durations and flip angles in the OVS [41] sequence remained unchanged.

3.5 Experimental Setup

Imaging was performed on a 3T Philips Achieva MR system (Philips Medical Systems, Best, The Netherlands) using a 12-element array spine coil. In-vitro To evaluate the performance of the OVS in combination with oblique SE selection the sequence was tested in phantom experiments. For this purpose, distilled water doped with paramagnetic contrast agent (Gd-DOTA; DOTAREM®; Laboratoire Guerbet, France) to have a T_1 1160 ms, and vegetable oil with T_1 290 ms were placed in a rectangular compartment of 225 mm in length. The phantom was first scanned with a full FOV of 240×240 mm^2 and a matrix size of 186 in a transverse orientation (fat-shift direction = anterior). To avoid excessive susceptibility effects a T_2 weighted segmented-EPI sequence was used. The intended reduced FOV of 30 mm was placed in the center of the phantom. Slice thickness was set to 2.5 mm, for tilt angles of 4.7°, 9.4° and 90° degree, corresponding to scanning in 2 packages, 3 packages and a single slice respectively. For the non-single slice scans, the number of slices was set to 3 per package with TR = 4000 ms. Three sets of images with oblique SE selection were acquired, once without OVS and SPIR, once with OVS but without SPIR, and once with OVS and SPIR. To evaluate the effect of oblique SE selection and the additional application of the OVS, line profiles in phase direction covering the entire image (with and without OVS) were generated from the water compartment of each image set. Additionally, signal intensities in the outer volume were determined in the oil and water compartment. To test the accuracy of the method, DTI data was acquired on a strand consisting of dyneema fibers mounted in a water filled cylinder [45]. The phantom provides homogeneous anisotropic diffusion over the entire cross-section of the strand, which was aligned in head-feet direction.

To simulate extensive outer volume tissue, water bottles were placed on the left and right side of the cylinder. DTI data of the phantom was acquired using the proposed reduced FOV approach in a transverse plane with the fold-over direction set to left-right. As a reference standard SS-EPI data of the same slice was acquired with the fold-over direction set to anterior-posterior on a coarser resolution to keep susceptibility distortions acceptable. The number of averages of both sequences was adjusted to match their relative SNR. ADC and FA values were evaluated for two ROIs placed inside the strand and in the bulk water region.

3.6 In-vivo

Using the described rFOV SS-EPI sequence with OVS and oblique SE selection, diffusion tensor data of the spinal cord were acquired in cervical, thoracic and lumbar regions, centering the imaging stack at level C5, T5 and at the level of the lumbar enlargement (T10-L1) respectively in 4 healthy subjects each. Depending on the size of the pathology the routine clinical conventional images in the axial plane range between 3-5 mm. Considering that the lesion conspicuity is higher on DTI, a slice thickness of 5 mm was chosen. To achieve time efficient acquisition in only two packages a tilt-angle α of 9.4° was used. Diffusion encoding was carried out in 6 non-coplanar directions $(-2/3, -1/3, -2/3)^T$, $(1/3, 2/3, -2/3)^T$, $(-2/3, 2/3, 1/3)^T$, $2^{-1/2} \cdot (1, 1, 0)^T$, $2^{-1/2} \cdot (0, -1, -1)^T$, $2^{-1/2} \cdot (1, 0, -1)^T$ optimized for the physical gradient system to achieve short diffusion gradients and thus, short echo time. A balanced gradient scheme was used to minimize eddy current effects. To achieve more accurate diffusion measurements [46, 47] and to avoid the problem of a temporal incoherence of the EPI-phase correction, acquisition was cardiac triggered after approximately 1/3 of the RR-interval where a period of relative motion quiescence is expected [36]. Further scan parameters were: NEX = 6 / 12 for b = 0 / b = 750 s/mm2, acquisition matrix = 176 × 44, FOV = 120 × 30 mm^2, $TR = 3000$ ms (3 or 4 cardiac cycles depending on the heart-rate), echo time (TE) = 49 ms, 60 % partial-Fourier acquisition. Maximal readout phase bandwidth was chosen to keep acquisition time short resulting in a read-out duration of 54.4 ms. Using multiple-slice interleaving, the scan time per slice was around one minute, covering a region of interest of 3 cm without slice gap in roughly 6 min (dependent on heart rate). Residual eddy current induced image distortion was reduced using a 2D-affine registration algorithm [26]. From these datasets, the mean apparent diffusion coefficient (ADC), relative anisotropy (RA) and fractional anisotropy (FA) [27] maps were calculated. The diffusivity values were evaluated separately for GM and WM in the cervical and lumbar datasets. Segmentation was performed manually after close consideration of anisotropy and DW images. Due to its smaller size and due to its very small fraction of grey matter, evaluation in the thoracic level was performed for the entire transverse cross-section of the spinal cord.

3.7 Results

3.7.1 In-vitro

Compared to a coplanar SE image showing the entire phantom (Fig. 3.3a), a tilting of 4.7° shows a reduced SE selection domain in the center of the FOV (Fig. 3.3b). The corresponding line profiles (Fig. 3.4a) spanning the entire image show the expected trapezoid signal profile for tilt angles $\alpha = 4.7°$ and $\alpha = 9.4°$, and an almost rectangular signal profile for a tilt angle of $\alpha = 90°$; spectral side lobes of the excitation pulse are apparent for all 3 tilt angles, and are particularly visible for $\alpha = 90°$. The additional application of the OVS, removes the unwanted SE selection domain transitions (Fig. 3.3c) including signal from the spectral side lobes of the excitation pulse. The corresponding line profiles (Fig. 3.4b) show a reduction of signal intensity to noise levels in the entire OV, while the homogeneous signal level (SNRoil = 62.3, SNRwater = 174) in the center part of the SE selection domain remained unaffected. The application of SPIR fat suppression efficiently removed signal from the lipid compartment (Fig. 3.3d). Signal loss related to slice cross-talk was not apparent in the signal profiles (Fig. 3.4).

In the strand region of the diffusion phantom the quantitative values of the reduced FOV acquisitions (FA $= 0.295 \pm 0.048$; ADC $= 1.42 \pm 0.07$ (437 voxel)) and the full FOV acquisitions (FA $= 0.297 \pm 0.06$; ADC $= 1.48 \pm 0.07$ (362 voxel)) were equal within in vivo measurement accuracy. In the bulk water region isotropic diffusion was measured for our reduced FOV approach (FA $= 0.031 \pm 0.009$ (500 voxel)) and the reference method (FA $= 0.029 \pm 0.010$ (453 voxel)). Slightly higher ADC values (ADC $= 2.24 \pm 0.02$) for the reduced FOV acquisitions as compared to the reference acquisitions (ADC $= 2.19 \pm 0.02$) were measured in the water region, which

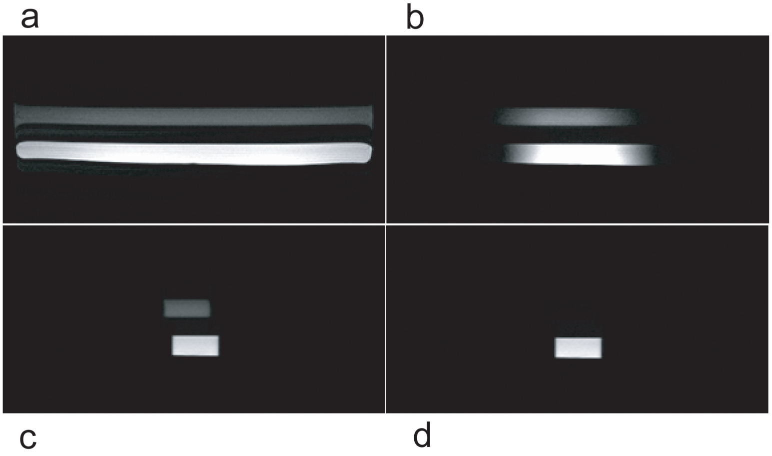

Figure 3.3: Interleaved EPI images showing the effect of the different modules on a phantom filled with water (below) and oil (above). The lipid compartment is displaced relative to the water due to water-fat shift. (a): Regular SE-EPI images with $\pi/2$ and π pulses applied in the imagining plane without OVS or fat suppression. (b): The $\pi/2$ pulse is tilted by $\alpha = 4.7°$. (c): As (b) with OVS suppression added to suppress the ramps of the signal profile. (d): As (c) with addition of SPIR fat suppression to remove lipid signals that may give rise to water-fat shift artifacts in the in-vivo experiments.

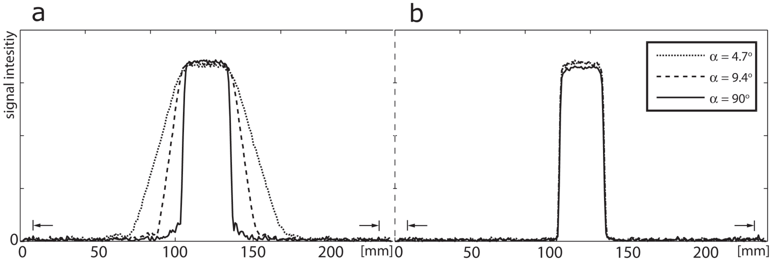

Figure 3.4: The effect of slice selection gradient tilting with (b) and without (a) OVS on the signal profile measured in the water compartment of the phantom. The arrows mark the extent of the phantom. (a): Showing the homogeneous central part of the SE selection and the residual signal from the transition in the SE selections including spectral side lobes of the excitation pulse. The transition width in the SE selection profile narrows for $|sin(\alpha)| \rightarrow 1$. Even for $\alpha = 90°$ the spectral side lobes of the excitation pulse are clearly visible in the signal profile. (b): The OVS suppresses all unwanted signal to noise levels while achieving narrow transition widths.

may relate to temperature changes during scanning.

3.7.2 In-Vivo

In-vivo images were virtually free of motion, susceptibility and aliasing artifacts in the area of the spinal cord (Fig. 3.5). Nerve roots were slightly visible in the cervical and lumbar mean DW images (Fig. 3.5) where nerve tissue has good contrast against the dark appearing cerebro-spinal fluid surrounding the spinal cord. As compared to T2 and ADC images, the mean DW images also enable moderate GM-WM differentiation. GM-WM contrast was best visible in the anisotropy images in the cervical and lumbar regions (Fig. 3.5) while the GM compartment is difficult to identify in the thoracic images. In agreement with spinal cord anatomy, the main eigenvectors are orientated cranio-caudally along the white matter tracts (Fig. 3.5). The measured quantitative diffusivity values averaged over each region of interest are listed for each subject in Table 3.7.2.

Region		FA μ,σ	RA μ,σ	ADC μ,σ [10-3mm2/s]
Cervical cord - GM	Subject 1	0.48 ± 0.13	0.43 ± 0.14	0.87 ± 0.10
	Subject 2	0.50 ± 0.10	0.45 ± 0.11	0.89 ± 0.11
	Subject 3	0.50 ± 0.12	0.45 ± 0.13	0.87 ± 0.11
	Subject 4	0.49 ± 0.10	0.49 ± 0.11	0.87 ± 0.10
	Average	0.49 ± 0.11	0.45 ± 0.13	0.88 ± 0.11
Cervical spinal cord – WM	Subject 1	0.77 ± 0.07	0.82 ± 0.12	0.90 ± 0.11
	Subject 2	0.73 ± 0.06	0.75 ± 0.10	0.92 ± 0.09
	Subject 3	0.75 ± 0.08	0.78 ± 0.13	0.87 ± 0.10
	Subject 4	0.75 ± 0.09	0.79 ± 0.14	0.93 ± 0.10
	Average	0.75 ± 0.07	0.79 ± 0.12	0.91 ± 0.10
Thoracic spinal cord – GM & WM	Subject 5	0.73 ± 0.09	0.77 ± 0.15	0.87 ± 0.12
	Subject 6	0.68 ± 0.11	0.68 ± 0.17	1.01 ± 0.18
	Subject 7	0.72 ± 0.13	0.76 ± 0.21	0.90 ± 0.15
	Subject 8	0.62 ± 0.10	0.60 ± 0.14	1.01 ± 0.13
	Average	0.69 ± 0.11	0.70 ± 0.17	0.93 ± 0.15
Lumbar spinal cord GM	Subject 9	0.29 ± 0.11	0.25 ± 0.11	0.85 ± 0.07
	Subject 10	0.34 ± 0.12	0.29 ± 0.11	0.92 ± 0.11
	Subject 11	0.33 ± 0.10	0.28 ± 0.09	0.84 ± 0.12
	Subject 12	0.32 ± 0.10	0.28 ± 0.09	0.87 ± 0.15
	Average	0.32 ± 0.11	0.27 ± 0.10	0.87 ± 0.11
Lumbar spinal cord WM	Subject 9	0.64 ± 0.07	0.62 ± 0.10	0.94 ± 0.11
	Subject 10	0.62 ± 0.09	0.60 ± 0.11	1.02 ± 0.16
	Subject 11	0.63 ± 0.08	0.62 ± 0.12	0.86 ± 0.12
	Subject 12	0.63 ± 0.08	0.62 ± 0.11	0.87 ± 0.13
	Average	0.63 ± 0.08	0.61 ± 0.11	0.92 ± 0.13

Table 3.1: Diffusivity values measured in the different regions of the spinal cord in healthy subjects.

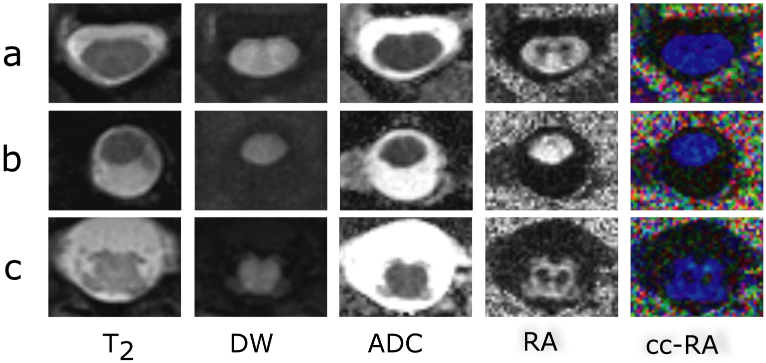

Figure 3.5: Diffusion tensor data of a healthy spinal cord at level C5 (a), T5 (b) and L1 (c) in the transverse plane. Displayed in the different contrasts are (from left to right): $T_2(b_0)$, isotropic DW, ADC, RA and color-coded RA (color coding: blue=head-foot, red=left-right, green=anterior-posterior direction).

3.8 Discussion

A novel reduced FOV approach for multislice SE sequences was introduced that combines OVS with an oblique SE selection, yielding an excitation with a nearly perfect rectangular profile to provide maximal signal for multiple-slice imaging. In-vitro experiments showed complete elimination of unwanted transition zones and OV signals for oblique SE selection. In particular, the evaluation showed less OV signal as compared to the perpendicular application of the excitation pulse stemming from spectral side lobes of the excitation pulse. By utilizing highly selective broadband pulses, the OVS remains robust in the presence of B_0 inhomogeneities, while being optimized to achieve efficient suppression in the presence of in-vivo B_1 variations for the range of in-vivo tissue T_1. Thus, no artifacts related to insufficient IV selection and OV suppression were visible in either the in-vitro or in-vivo datasets. The accuracy of the method was confirmed by matching diffusitivity values in the reference measurements on a diffusion phantom. Due to the shortened readout duration, in-vivo images were virtually free from off-resonance artifacts, while enabling short echo times and reduced T2* blurring despite the small voxel sizes. The acquired images, having an in-plane resolution of 0.7 mm2, depict fine anatomical details in all assessed contrasts (T2, DW, ADC, anisotropy) showing good GM-WM contrast in the cervical and lumbar anisotropy images.

3.8.1 Diffusitvity values

Reviewing current literature, very few publications have hitherto mentioned diffusitivity values in the thoracic spinal cord [48] or separate values for GM and WM in the cervical region [28, 41, 49, 16]. To the authors knowledge there have been no publications mentioning lumbar spinal cord DTI values, which likely to be related to the strong B_0 inhomogeneities and problematic shimming in the lower spinal cord. A brief discussion on cervical whole spinal cord diffusitivity values is given in ref. [41]. A recent publication [49] presented mean anisotropy measures in cervical GM (FA = 0.45) and WM (FA = 0.69 - 0.79) similar to the values given in this paper.(FA(GM) = 0.49; FA(GM) = 0.75). Measured anisotropy values in the cervical GM were lower (FA = 0.49) than previously reported [41] (FA = 0.56). We attribute this to diminished partial volume effects in the present high-resolution, minimally blurred images. Despite these improvements, the anisotropy values in cervical GM likely remains overestimated due to residual partial volume effects and errors in the co-registration., In the thoracic region the portion of GM is very small compared to the WM compartment such that the evaluation was not performed separately on GM and WM ROIs. The small fraction of GM also explains the relatively high anisotropy values (FA = 0.69) that were observed in the whole cross-section regions. It is well recognized that diffusitivity values are susceptible to noise contamination [50] that typically leads to an overestimation of FA and ADC. Particularly in some thoracic datasets shimming problems and resulting SNR loss may be reflect by increased anisotropy values (Table 1: subjects 5 and 7). Nevertheless the mean FA and ADC (= 1.0 10-3mm2/s) values are smaller than previously reported [48] (FA=0.75 / ADC =1.0 10-3mm2/s). In the lumbar spinal cord, the anterior and posterior columns of the GM are more expanded, which renders a more accurate evaluation possible. The diminished partial-volume effects are reflected in the lower anisotropy values (FA = 0.32). In accordance to previously acquired data [51] using line scan diffusion imaging, the lumbar WM compartment shows a decrease in diffusion anisotropy as compared to the cervical level. This likely reflects the progressive decrease in the number of long axons and the loss of their myelin sheath [52] as one moves caudally.

3.8.2 Oblique spine echo

For pulses applied in the phase encoding direction, the need of a preferably rectangular signal profile and high BW is essential to avoid inhomogeneous signal weighting within the FOV, unwanted OV excitation and spatial mispositioning due to B_0 inhomogeneity. These effects may impair image quality if a π pulse jeong2005, wheeler2002mrm or a 2D-selective pulse [42, 39, 40] is applied in phase encoding direction where the above mentioned pulse properties can be less easily achieved as compared to a $\pi/2$ pulse. Thus, the use of OVS may also be beneficial for approaches similar to the ones mentioned above. Note that a high quality excitation profile of the tilted pulse is also essential to minimize inter-slice cross-talk.

3.8.3 SNR, resolution, blurring

The rectangular inner volume profile minimizes the possible readout duration to achieve minimal T_2^* blurring and minimal off-resonance distortions for a given image resolution. Any readout prolongation will increase the aforementioned negative effects. Utilizing the time efficient acquisitions using only two packages without gap, an approach using oblique SE approach without OVS [17] will require a more than two fold increase of EPI readout duration. Considering the well known SNR equation, , the approach benefits from high field (3T) acquisition that overcompensates for the necessary readout duration shortening in order to compensate for the stronger off-resonance. For typical matrix sizes further SNR is gained by the enabled TE shortening (note the relatively constant T_2 at 3T as compared to lower field (1.5 T) [53]). In other words, any readout duration decrease can be traded in for an acquisition at higher field strength that will increase the achievable SNR. The oblique SE selection constraints a gap-less volume to be scanned in two packages, which doubles the minimal overall scan time for a fixed TR. For acquisition of only few slices, where the two TRs cannot be fully utilized for acquisitions, the sequence will not achieve full SNR efficacy, similar to a perpendicular volume selection case [18]. Thus, in a worst case the maximum scan time per slice is 3 minutes. For typical spinal cord applications however, where several slices are used to cover an expanded region in head-foot direction, full SNR efficacy is achieved. In this case the scan time per slice is reduced to less then 1 minute depending on the SAR limitations that currently constraints our acquisition to one SS-EPI readout in 675 ms. This implies no restrictions on acquisition speed for cardiac triggered acquisition (frequency $\leq$ 88 beats/minute), which is considered to improve the accuracy of the obtained diffusitivity values [46] and motion robustness of the sequence - in particular minimization of Nyquist ghosts that may arise due to inconsistent motion during EPI reference scan and image acquisition. For faster non-cardiac triggered acquisitions we suggest implementing OVS by two pulses per slab, which enables to acquire 25 % more slices in the same time. Comparing the proposed method to other existing DWI techniques, interleaved EPI (not suffering from the disadvantages mentioned above) has not shown to achieve comparable results for spinal cord imaging due to its sensitivity to motion. Line scan imaging has been shown to achieve similar image quality and resolution but requires relatively long scan times (13-16 minutes per slice [16]). Compared to SS-EPI parallel imaging approaches, that may be used for cervical imaging regions on lower field strengths improved SNR is achieved for the same reduction of acquired k-space lines. This paper limits itself to diffusion imaging of the spinal cord. However, this technique may be applied to other anatomical regions and furthermore may be practical for DW imaging at even higher field strength.

3.9 Conclusions

We introduced a novel reduced FOV approach for diffusion weighted imaging by a combination of oblique SE selection and OVS. The achieved SS-EPI readout reduction enables high-resolution acquisition in the entire spinal cord. The technique gains from the insensitivity of its inner volume selection with respect to B_0, B_1 and tissue T_1 variations. In-vivo imaging was performed in the cervical, thoracic and lumbar spinal cord in the transverse orientation. Acquired data was reproducibly free from motion and susceptibility artifacts. For the cervical and lumbar level, the improved resolution of the DTI data enabled separate evaluation of the GM and WM compartments. The short imaging time makes this approach readily applicable for clinical studies of the spinal cord.

Chapter 4

A transmit receive system for magnetic field monitoring of in-vivo MRI

4.1 Introduction

Most in-vivo MR experiments rely on signal encoding by magnetic fields that vary in both space and time. The accurate interpretation of the resulting signals requires accurate knowledge of the spatiotemporal field evolution during the experiment. The first and foremost means of ensuring such reliability is optimizing the hardware used for generating the desired field evolution [54, 55]. Remaining hardware inaccuracies can sometimes be addressed by judicious sequence design [56, 57]. A generic alternative is measuring reproducible field imperfections and pre-correcting gradient waveforms [58, 59, 60] or post-correcting the MR data at the signal processing level [61, 62, 63, 64, 65, 66, 67, 68, 69].

Despite these refinements advanced MR methods are still hampered by residual field imperfections that cannot be fully addressed by hardware calibration and error prediction, including long-term drifts and non-recurring field changes such as those from breathing or limb motion [70, 71]. To address this issue it has recently been proposed to monitor the actual field evolution concurrently with any MR sequence [72]. In this approach miniature NMR probes [73, 74, 75, 76, 77, 78] are used to record the phase evolution of MR signals originating from a set of positions around the imaging region. Based on these data a global phase model is calculated that can then be used as a basis for processing the actual image or spectroscopic data.

The field monitoring approach has thus far been demonstrated for phantom imaging with fast readouts of gradient echoes [72], using receive-only NMR probes. While proving the monitoring principle the receive-only approach has important limitations. Firstly, receive-only probes need to be excited by radiofrequency (RF) transmission through an external volume coil, which may interfere with the actual MR experiment. Secondly, external RF pulses required to manipulate the magnetization in the imaged object may conversely perturb the probe magnetization. And thirdly, being sensitive to external fields such probes are prone also to receiving MR signal from the object or subject under investigation, which corrupts the monitoring result. In the previous demonstrations these issues were addressed by exciting both the probes and the object by suitable spatially selective RF pulses and by sufficient geometrical spacing between NMR probes and the object. This approach will hamper the routine use of field monitoring for in-vivo applications, which requires full freedom of slice and volume position and orientation. In-vivo imaging practice also limits the freedom of placing field probes and often requires more intricate pulse sequences with multiple and potentially strong RF pulses during a single sequence repetition.

All of the described limitations of receive-only probes are related to RF interference between the actual imaging experiment and the probes, be it at the excitation or the reception stage. The goal of the present work is to solve this issue by mutually isolating the main experiment and the operation of the field probes with respect to RF fields. This is achieved by the introduction of transmit/receive (T/R) NMR probes that are RF-shielded and excited by a separate RF chain. It is demonstrated that the T/R approach enables robust and highly accurate field monitoring of in-vivo scans, involving multiple slice positions and orientations as well as spin-echo sequences.

4.2 Field Probes

4.2.1 Sample and RF coil

Like the previously described receive-only probes [76] the new probe head is based on a liquid NMR sample contained in a glass capillary and surrounded by a solenoid detector coil (Fig. 4.1). The capillary has been miniaturized to an inner diameter of 800 μm, enabling the monitoring of scans with higher image resolution. The resulting sensitive volume is below 300 nl, requiring maximum-sensitivity detection. To this end the capillary wall is very thin (100 μm) and the solenoid fits tightly on the capillary for maximal filling factor. The solenoid is wound from enameled copper wire 90 μm in diameter.

4.2.2 Droplet formation

The capillary limits the NMR sample only in two dimensions, requiring some additional means of forming a droplet with an equally small diameter also in the third dimension. In previous capillary probes [76, 78] this was accomplished by surrounding the active droplet with plugs of another liquid that gives no NMR signal at the probe's operating frequency. To prevent line broadening the magnetic susceptibility of these plugs was matched to that of the droplet [79]. While successful in practice, the plug approach entails demanding manufacturing and constrains the choice of the two liquids involved. The sample and plug liquids should exhibit surface tensions that cause the NMR sample to form a favorably convex rather than concave droplet. The two liquids, with any agents dissolved therein, must also be chemically inert and immiscible. This requirement constrains the possibility of adjusting the relaxation rates in the droplet and the room for susceptibility matching. The latter is difficult for water droplets, which are more diamagnetic (-9.05 ppm SI volume susceptibility) than most other liquids.

The difficulties of the plug approach can be circumvented with T/R probes, which open up an alternative way of confining the sensitive volume in the third dimension. An effective droplet can also be formed by the combined spatial selectivity of the solenoid's transmit (B_1^+) and receive characteristics (B_1^-). For this approach the capillary may be filled homogeneously with a single liquid. This option not only simplifies manufacturing but also overcomes all requirements on liquid compatibility, leaving a larger choice of sample liquids and dopants. In particular, it facilitates the use of H_2O samples, which combine high proton density with favorable solvent properties. Due to these advantages water samples were used throughout this work. To implement B_1 -based droplet formation short solenoids of only 3 turns were used, yielding an inductance of 28 nH.

4.2.3 T_1 adjustment

For repeated probe excitation at high rates it is beneficial to reduce the T_1 of the probe sample while keeping its T_2 as large as possible. For water samples this can be readily achieved by adding copper sulfate pentahydrate ($\mathrm{Cu(II)SO_4{\cdot}5H_2O}$). To reach T_1 and T_2 of approximately 100 ms, a concentration of 3.3 g/l was chosen, extrapolating literature data available for 63 MHz [80].

4.2.4 Casing

For sealing, mechanical robustness and ease of use the capillary and solenoid are embedded in a solid casing. To avoid line broadening of the sample the casing material must be susceptibility-matched to the specific copper wire used [74, 76]. To this end a suitable two-component epoxy system (Swiss Composite, Jegenstorf, Switzerland) was identified using the susceptometry method described in Ref. [81]. Adverse susceptibility effects must also be prevented when choosing the shape of the casing. According to magnetostatics any homogeneous, magnetically susceptible ellipsoid, when placed in a homogeneous magnetic field, will give rise to a homogeneous net field inside itself [82]. Consequently the net field will still be homogeneous in the innermost of a set of nested ellipsoids as long as each is of homogeneous and low susceptibility. In the described probes the sample liquid and glass capillary form nested long cylinders, which are good approximations of prolate ellipsoids. Following the same logic the casing should ideally again be ellipsoidal. Therefore the epoxy jacket was cast into an ellipsoid closely fitting the length of the capillary (Fig. 4.1).

4.2.5 Tuning and matching

The solenoid is resonated at 127.8 MHz for operation at 3T, using balanced tuning by two variable capacitors. The capacitors are housed in a small box several centimeters away from the probe head to prevent them from

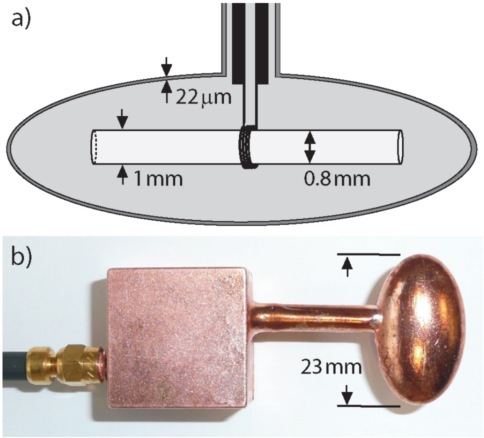

Figure 4.1: a) Schematic of the T/R probe head. The sample capillary, solenoid and ellipsoidal epoxy casing are surrounded by a 22 μm copper shield. The thin wire forming the solenoid is connected to a thicker wire of lower resistance. b) Photograph of a shielded probe head (rotated by 90° relative to the schematic), including the tuning/matching box and the connection to the coaxial cable.

disturbing the field homogeneity in the sample. The solenoid is connected to the tuning capacitors by 1-mm-thick, silver-plated copper wire to minimize losses (Fig. 4.1). A third variable capacitor, housed in the same box, serves for matching to a shielded 50-Ω coaxial cable that connects to a T/R switch.

4.2.6 RF Shield

RF shielding of the probe head is achieved by plating it with a layer of copper [83]. In order for external RF fields not to penetrate the shield, its thickness must amount to at least several multiples of the RF skin depth in copper, which is 5.8 μm at 127.8 MHz [84]. Conversely, the conducting layer should be as thin as possible to provide a high resistance to low-frequency currents that will be induced by gradient switching. Such eddy currents, if significant, will partly shield the gradient fields and thus worsen the fidelity of the monitoring measurement. To reconcile these goals a copper shield of 22 μm thickness was applied, using electroplating. The shield encloses the probe head, the tuning and matching box, as well as the connection between them. It is connected to the shield of the coaxial cable through a small connector of the SMC family (Huber+Suhner, Herisau, Switzerland).

4.3 Driver Hardware

4.3.1 Receive path

Integrated on a T/R board, the T/R switch is based on actively-biased PIN diodes [85] and performs the function of switching between RF transmission and reception. This board also includes a low-noise preamplifier for boosting the weak probe signal. The T/R board is made of 1.5-mm-thick double-sided fiberglass (FR4) circuit board and is enclosed within an RF-shielded box shorted to the shield of the incoming coaxial cable. Each probe's receive output was connected to an individual channel of a 32-channel Achieva spectrometer (Philips Healthcare, Best, The Netherlands). Further inputs of the same spectrometer were used to connect an 8-channel head receive array (Invivo Corporation, Orlando, FL), enabling strictly synchronous sampling of probe and image data.

4.3.2 Transmit path

The field probes are excited through a separate transmit path independent from that of the imaging system. Operating the probes independently requires high-bandwidth RF pulses that will reliably excite all probes irrespective of potentially strong gradient fields. Due to their small dimension the T/R probes described here permit generating such pulses with only small RF power. Block pulses of a few s in duration are generated with a pulse generator and modulated at 127.8 MHz by a frequency generator (both Hewlett-Packard, Palo Alto, CA). The pulses are then amplified by an RF amplifier with a pulsed power of up to 300 W (Model 3205, American Microwave Technology, Anaheim, CA). The RF amplifier is unblanked only during a time window that just contains the respective pulse. A maximum of 8 probes can be driven simultaneously by feeding the amplified pulse to an 8-way splitter based on a cascade of 7 quadrature hybrids [86]. Individual attenuators on each output channel permit per-probe flip angle adjustment. In the present work up to 4 probes were used simultaneously. 50 Ω loads terminated the remaining splitter channels. With this setup a total power of about 1 W is sufficient for 90° nutation in 5 μs.

4.3.3 Control

All experiments were performed on a 3 T whole-body MR system (Achieva, Philips Healthcare, Best, The Netherlands). The operation of the field probes was controlled along with the actual imaging sequence via the system's console. The latter was programmed to trigger probe excitation by a TTL signal that triggers the pulse generator and unblanks the RF amplifier. A separate console signal was used to control the T/R switches. In imaging experiments simultaneous data acquisition from all channels involved was started immediately after slice refocusing (gradient-echo sequences) or after the RF refocusing pulse (spin-echo sequences). Throughout, the probes were excited by 90° pulses immediately prior to the acquisition interval.

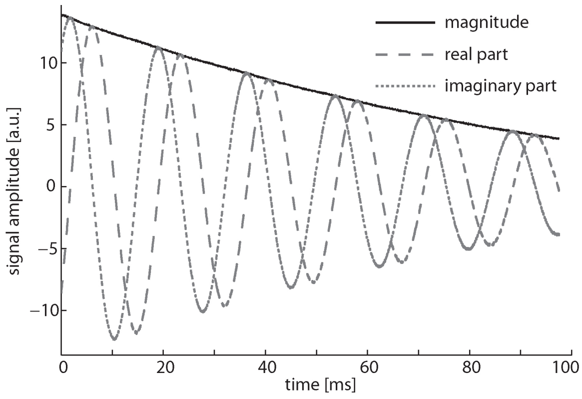

Figure 4.2: FID of a T/R field probe doped with 3.3 g/l of copper sulfate pentahydrate, acquired for 98 ms.

4.4 Performance Assessments

4.4.1 FID quality

Figure 4.2 shows a free induction decay (FID) signal obtained with a T/R probe, acquired after excitation in the fully relaxed state. After 98 ms the signal has decayed to 27% of its initial strength. Given that T_2 is approximately 100 ms this result confirms minimal inhomogeneous line broadening and thus a nearly perfect susceptibility match between the solenoid wire and the epoxy casing. Using the measure $\xi = SNR\sqrt{BW}$ [76], the FID reflects an initial probe sensitivity of $\xi = 7.110^4\sqrt{Hz}$. This value compares favorably with the maximal ξ values of $\xi = 2.010^4\sqrt{Hz}$ reported in Ref. [76] for a receive-only probe with a sample volume about four times larger.

4.4.2 T_1 adjustment

Upon repeated probe excitation with repetition times (TR) below a few multiples of T_1, the probe's sensitivity benefits from reducing its T_1. Table 4.4.2 shows the observed initial ξ for various TR, comparing a pure H_2O probe with one doped with $CuSO_4 \cdot 5H_2O$ (3.3 g/?). For fast repetitions T_1 adjustment improved the probe sensitivity by up to a factor of 4.

TR $[ms]$	50	100	200	500	1000	2000	5000
pure H_2O probe	1.1	1.4	1.8	3.0	4.1	5.6	7.8
$CuSO_4$-doped H_2O probe	3.9	5.6	6.7	8.5	8.9	9.0	9.1

Table 4.1: Probe sensitivity as a function of TR, compared for pure and $CuSO_4$-doped H_2O probes.

4.4.3 RF shield

To assess the effectiveness of RF shielding one shielded and one unshielded probe head were exposed to magnetic RF field in a bench test. Using a network analyzer, an S21 measurement was performed, transmitting with a tuned and matched solenoid coil (4 loops, 14 mm diameter) and receiving with the respective probe head. The unshielded probe was placed 52 mm above the solenoid coil and rotated such that the coupled signal was maximal (-38.1 dB). The shielded probe was then placed in the exact same position and orientation, yielding a coupled signal of -75.8 dB. The isolation of the shielded probe head was thus estimated at roughly -38 dB.

4.4.4 Isolation from object MR signal

The sensitivity of a probe to external MR signal was studied by an MR experiment, receiving probe signals in the presence of precessing magnetization in a nearby object. A shielded and an unshielded probe filled with D2O instead of H2O were placed symmetrically close to the bottom of a 5l water bottle. A 20-mm-thick slice at the bottom of the bottle was excited by a 90° RF pulse. The signal was then de- and rephased by a gradient, such that a gradient echo formed after 7.2 ms. The time evolution of the signal detected by the two probes is compared in Fig. 4.3. The unshielded probe shows a distinct gradient echo, reflecting substantial signal coupling from the bottle. The signal obtained simultaneously with the shielded probe reveals no visible contamination, suggesting effective shielding of object signals. This finding was confirmed by the subsequent imaging experiments, in which likewise no signal coupling through the probe shield was observed. Slight excitation of probe samples by the body coil still occurred when applying large flip-angle pulses on resonance. However, the resulting minor saturation of the probe magnetization was not critical.

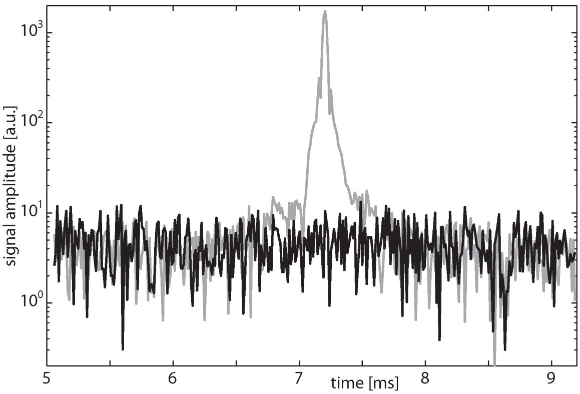

Figure 4.3: Contamination of the probe signal by MR signal of a nearby water bottle. The formation of a gradient echo is shown for an unshielded (gray) and a shielded probe (black) in a logarithmic scale.

4.4.5 Gradient eddy currents on the probe shield

The switching of gradient fields inevitably induces eddy currents on the probe shield. Due to the thin plating and small dimensions of the probe heads these eddy currents are small and short-lived. It may therefore be expected that their effect on the monitoring measurement is limited to a mere delay in the probe's phase response, an assumption that will later be tested by image reconstruction based on probe data. The assumed delay was determined experimentally by comparing the signal phase evolution of a shielded and an unshielded probe under the influence of a gradient blip. The two probes were placed point-symmetrically about the scanner isocenter in positions off-center in all three gradient directions. Probe data were acquired for 50 ms with a gradient blip of 0.5 ms played out at 40 ms. The initial 40 ms of these data were used to determine and correct for the individual probe's static off-resonance frequency. Then their phase was extracted and unwrapped and the initial phase offset was subtracted such that both probes' phase evolutions started at zero. Finally the second probe's phase time course was inverted in sign, due to its opposite position, and scaled to that of the first probe to account for slightly unequal distances from the isocenter. From the resulting phase time courses the relative delay of the shielded probe's phase was determined by least-squares fitting. Measurements of this kind were performed with blips in all three gradient directions. The delays measured for the x, y and z gradient direction were 4.88 μs, 4.73 μs, and 4.73 μs, respectively. This suggests that the delay was essentially independent of the direction of the applied gradient. Based on these findings all probe signals in the following were corrected for a 4.8 μs delay.

4.4.6 Droplet formation

A gradient-echo image taken with a T/R probe is shown in Fig. 4.4, revealing the successful formation of an effective droplet. In the following the behavior of such a droplet under the influence of gradient fields is examined. Figure 4.5 illustrates the dephasing behavior of the droplet along and perpendicular to the capillary. A probe FID under a read gradient perpendicular to the capillary shows the characteristic jinc-like* Fourier response of cylindrical objects. Along the capillary the droplet is not delimited by sharp physical borders but by the solenoid's smoothly decreasing B_1^+ and B_1^-. Applying a gradient along this direction leads to a signal drop-off in k-space without side lobes. However the range in k-space that can be covered with this probe is very similar in both directions, confirming the suitability of 3-turn solenoids at the wire thickness of 90 μm. According to this k-space range the current probes permit monitoring imaging sequences with spatial resolutions down to approximately 400 μm, as also indicated by the dashed line in Fig. 4.5.

4.4.7 Echo-Planar Imaging (EPI)

To show the feasibility and flexibility of concurrent image acquisition and T/R field monitoring, gradient-echo EPI scans were performed in a water phantom and a healthy volunteer. All built-in mechanisms for gradient correction and preemphasis were enabled. Four field probes were arranged around the 8-channel head array in an approximately tetrahedral fashion. In each setup the probe system was calibrated as described in Ref. [72], involving measurements of the probes' positions and static frequency offsets. For each EPI segment a first-order phase model was calculated according to Ref. [72], yielding the corresponding effective k-space trajectory. Based

---

*The jinc function is defined as a Bessel function of the first kind (J1) divided by its argument.

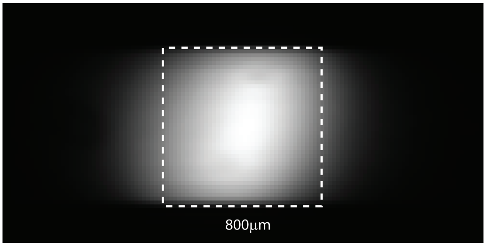

Figure 4.4: Spin-warp gradient-echo image of the effective droplet in a T/R probe. In-plane resolution = 40 μm × 75 μm; projection in the slice direction. The capillary is oriented horizontally.

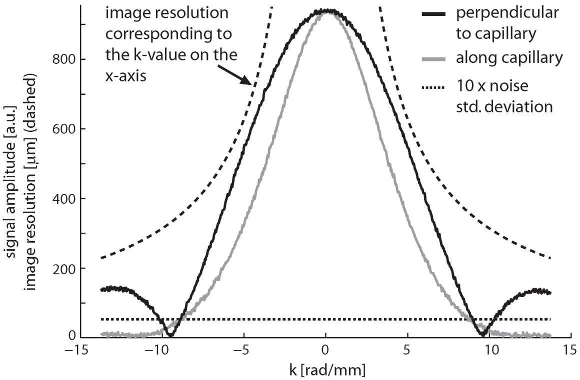

Figure 4.5: Dephasing of the probe signal under a gradient perpendicular to the capillary (black) and along the capillary (gray). The dash-dotted line marks a typical SNR threshold of 10, indicating equal k-space mapping ranges in the two dimensions. The dashed line plots the achievable image resolution as a function of k.

on this trajectory, image reconstruction from the 8-channel head data was performed, channel by channel, using a standard gridding algorithm. An array image was then obtained by standard root-sum-of-squares combination.
Initially, segmented EPI was performed in the phantom to study the effect of field monitoring on artifact behavior. Based on the same set of EPI data an array image was reconstructed first on the basis of the concurrently measured k-space trajectory and then, for comparison, in a conventional fashion. For the conventional reconstruction the k-space trajectory was replaced by the nominal one according to the gradient waveforms defined on the console. In keeping with most conventional implementations of EPI reconstruction the residual delay of the frequency encoding gradient, causing data inconsistency between forward and backward profiles, was corrected for based on calibration data. However the correction was minimal and left the resulting image virtually unaffected. Figure 4.6 shows the resulting images in a logarithmic scale to emphasize artifacts in the background. As seen there the conventional image exhibits small but distinct ghosting artifacts, indicating slight imperfections of the effective k-space trajectory. By contrast the image obtained with field monitoring is free of ghosting. The difference of the two images, in a linear scale, reveals slight artifacts also within the phantom. The underlying differences between the measured and nominal k-space trajectories are also shown, for one EPI segment and separately for the phase- and frequency-encoding directions.

All of the following results were obtained by monitoring-based reconstruction. Figure 4.7 shows a selection of in-vivo images for various slice orientations and positions, readout durations, and degrees of EPI segmentation. Except for minor motion artifacts in the sagittal views these results are also free of conspicuous errors. In particular, like in the previous phantom image there is no sign of ghosting as one would expect even from very minor relative delays between the assumed and actual k-space trajectory. This corroborates the assumption of a simple delay of probe data due to gradient eddy currents on the probe shields. Moreover the data confirms that the delay model is generally applicable since the same delay correction was successfully applied to data sets of different orientations, resolutions, and degrees of segmentation. To demonstrate the tolerance of the shielded T/R system against multiple and strong RF pulses in the imaging sequence, a second set of tests was dedicated to segmented spin-echo EPI in

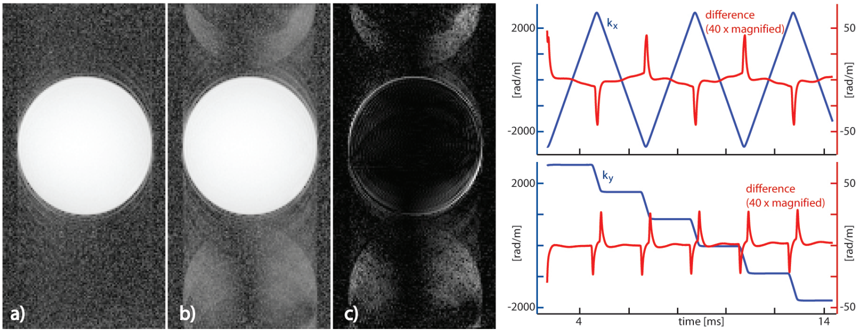

Figure 4.6: Segmented gradient-echo EPI, reconstructed based on (a) the concurrently measured and (b) the nominal k-space trajectory (both in logarithmic scale). (c) Difference be-tween these images (linear scale). The plots on the right show the measured k-space time courses of one EPI segment in the (top) frequency- and (bottom) phase-encoding direction, along with their differences from their nominal counterparts (in a zoomed scale). EPI sequence: 32 interleaves / 6 echoes, $TE = 9.7\ ms$, $T_{acq} = 15.6\ ms$, resolution $= 1.2\ mm$.

a phantom and in vivo (Fig. 4.8). Again ghost-free reconstruction confirms accurate field monitoring.

4.5 Discussion and Conclusion

The proposed T/R monitoring system renders field probing during MR procedures robust and flexible and has enabled the first in-vivo demonstrations of MRI with concurrent spatiotemporal field monitoring. Compared with the previous receive-only implementation the advantages of the T/R approach are manifold. The need to fit probe excitation pulses into the imaging sequence is overcome by the RF independence of the probe and imaging experiments. The separate probe transmit chain also affords maximal flexibility of timing the probe excitation, which is helped by its ability to achieve pulse bandwidths of many hundreds of kHz. The timing of data acquisition has so far been kept identical for the probes and imaging coils to limit changes to the spectrometer software. The related minor limitations could be overcome by acquiring the probe data with separate

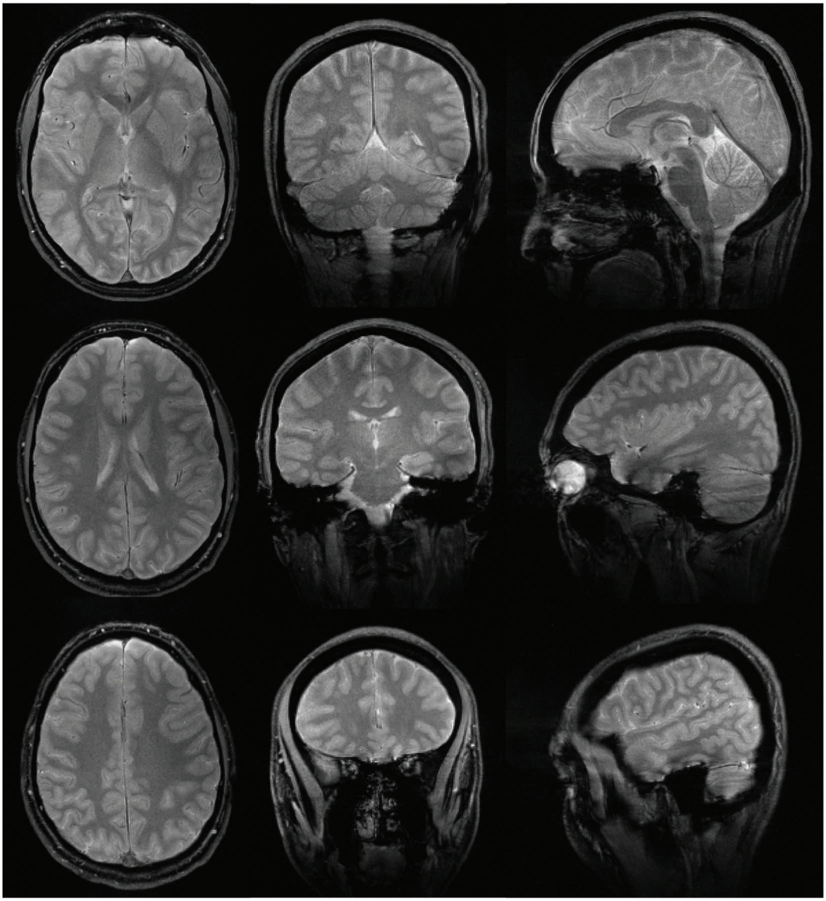

Figure 4.7: Segmented gradient-echo EPI, reconstructed based on probe data. Transverse (left): 36 interleaves / 8 echoes, $TE = 12.6$ ms, $T_{acq} = 18.9$ ms, resolution = 0.8 mm. Coronal (mid-dle): 58 interleaves / 4 echoes, $TE = 6.8$ ms, $T_{acq} = 9.4$ ms, resolution = 1 mm. Sagittal (right): 72 interleaves / 4 echoes, $TE = 7.3$ ms, $T_{acq} = 10.3$ ms, resolution = 0.8 mm. Slight artifacts in the sagittal views are due to eye motion and CSF pulsation.

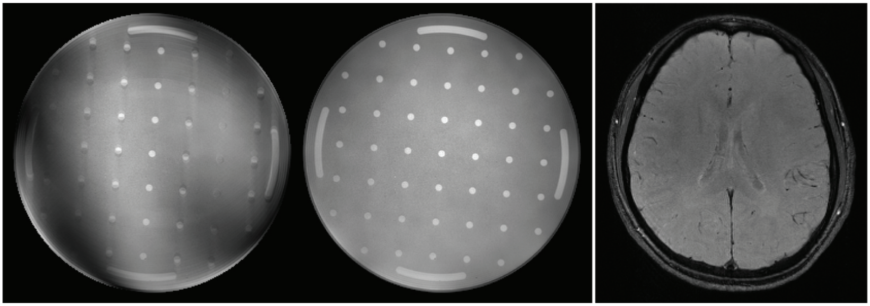

Figure 4.8: Spin-echo EPI in a phantom and in vivo. 50 interleaves / 6 echoes, TE = 30.3 ms, T_{acq} = 13.3 ms, resolution = 0.8 mm. The left phantom image was obtained without correcting for the delay caused by the probes' RF shields (4.8 μs). Comparison of the two phantom images illustrates the importance and accuracy of this correction.

receiver hardware synchronized to the main system. B_1-based droplet formation in a homogeneously filled capillary simplifies manufacturing, removes constraints on the choice of the sample liquid and facilitates T_1 and T_2 adjustment, while naturally yielding perfectly uniform susceptibility inside the capillary. The ellipsoidal epoxy casing preserves the homogeneity of the external magnetic field and thus maximizes the probe signal lifetime in conjunction with susceptibility matching to the RF solenoid. The probe heads have also been further miniaturized, permitting the monitoring of k-space trajectories down to a nominal image resolution of approximately 400 μm. The use of smaller effective probe droplets relies critically on thorough RF shielding that virtually eliminates signal contamination by object signal. Shielding as described in this work also enables positioning the probes in arbitrary geometrical positions and close to the object, imaging thick slices or 3D volumes, arbitrary slice orientations, and spin-echo scans.

Gradient eddy currents on the RF shields are per se an adverse effect. However, due to their short lifetimes they can be modeled as causing a simple delay of the MR phase evolution in probe droplets. Successful correction for this delay has been demonstrated by ghost-free EPI reconstructions. It is noteworthy that the observed delay is practically independent of the direction of the underlying switched fields. This is plausible considering that only eddy currents in the transverse plane, giving rise to magnetic field parallel to B_0, will considerably perturb the field magnitude in the probe sample. Closer analysis may yield a more elaborate model involving anisotropic transfer functions [87].

A promising design alternative is using a different nucleus for NMR in the field probes, which will overcome RF interference with proton experiments by spectral separation. Not requiring an RF shield, non-proton probes will be simpler to manufacture and free of eddy current perturbations, but require multiple-frequency capability of the spectrometer. Otherwise the hardware and methods described here will apply straightforwardly to non-proton probes. Continued development of the described T/R probes should also target further miniaturization and SNR optimization. Promising uses of T/R field monitoring include enhanced image reconstruction and real-time feedback to gradient and shim systems. The latter will be useful for tackling field perturbations that cannot be fully addressed at the signal processing stage.

Chapter 5

Integration of higher-order dynamic fields into MR image reconstruction

5.1 Introduction

Since the early days of MRI, gradient systems of MR scanners are designed to create spatially linear gradient fields. Spatially linear image encoding helps to achieve good conditioning of the reconstruction problem, and provides Fourier reconstruction as an efficient reconstruction algorithm. Despite major efforts gradient systems still show significant temporal and spatial deviation from the pre-described behavior. In particular dynamic higher-order fields are created.

There are several potential sources of dynamic higher-order magnetic fields*. Gradient fields are necessarily accompanied by changes of **B** in the transverse plane, a consequence of Maxwell's equations. These trans-

---

*In physics textbooks, the magnetic field **H** is distinguished from the magnetic induction $\mathbf{B} = \mu_0(\mathbf{H}+\mathbf{M})$, where the magnetization **M** of the material is itself a function of **H** [88].

verse field changes contribute to B and are called *concomitant fields* [89]. They are of second and higher order in space and – unlike the static gradient non-linearities – scale non-linearly with the applied gradient strength. Another source of of dynamic 0^{th}, 1^{st} and higher order fields which are particularly difficult predict, are *eddy currents* induced in various conducting structures such as the gradient coils, the cryostat, the main magnet or the shim coils. Eddy currents grow with increasing gradient strength and slew rate. Finally *thermal effects* in magnetized parts of the scanner such as the shim irons may cause long-term field drifts leading to slowly varying and potentially non-linear field drifts.
Unaccounted effects on the signal phase accumulate over time, thereby amplifying spurious effects in long readouts. Moreover off-center regions are affected more drastically by higher-order fields.

Dynamic higher-order fields lead to a large variety of image artifacts. They result from the cumulated effects of imprecise knowledge of the fields, the k-space acquisition strategy and the chosen reconstruction algorithm. Prominent examples are image warping in Cartesian- [67] and blurring in spiral imaging [90].
While acceptable for diagnosis on the basis of anatomical (T_1-, T_2- or proton-density-weighting) images, image distortions are particularly problematic in cases where data fusion of more than one MR image is necessary. Errors imposed by the geometrical mismatch of images will propagate to derived measures such as in diffusion imaging [27], B_0 mapping, magnetization transfer imaging [91], functional MRI time-series and can severely impede B_0 correction as well as parallel imaging [30]. Thereby already small deviations of the spatial encoding can impose drastic limitations in terms of image resolution and accuracy.

Several approaches have been suggested to tackle dynamic higher-order field effects. Eddy currents can be reduced by means of sequence design, mostly used in diffusion imaging [56, 57, 92], however not without compromising SNR efficacy while still accepting residual errors. For constant linear velocity spirals it was proposed to incorporate concomitant field correction into the static B0 conjugate phase reconstruction [68]. Phase correction of concomitant field effects is regularly performed in phase contrast measurements [90]. The correction of global image distortions can also be performed in a post-processing step such as image co-registration

[93, 26], however, the resulting geometrical fidelity is not always satisfactory.

To generically approach the problem of dynamic higher-order fields, an image reconstruction algorithm is proposed that deliberately tolerates a certain degree of higher-order fields, and rather accounts for them by their direct integration into image reconstruction. Clearly the approach requires exact knowledge of the field evolution during the imaging experiment. The recent invent of long living NMR probes [94] allows for fast and accurate measurement of spatiotemporal field evolution. Provided a suffcient number of probes also higher-order fields can be captured [95]. The aim of this work is to describe a generalized approach to image reconstruction that accounts for dynamic higher-order fields. Image reconstruction is solved as a general inversion problem [96]. Leaving the realm of Fourier encoding not only requires new formalisms to describe spatial encoding, but also complicates image reconstruction by posing a non-unitary problem. To show the necessity of knowledge and correction of dynamic higher-order fields we show the improved congruence of variably diffusion weighted images acquired in phantom measurements and additionally present in-vivo results.

5.2 Theory and Methods

5.2.1 Spatial encoding

In MRI spatial information is encoded by spatial and temporal magnetic field B variation which manipulates the magnetization phase. At each location $\mathbf{r}$ and each time point t after excitation the phase ϕ of the magnetization is given by

$$\phi(\mathbf{r}, t) = \gamma \int_0^t B(\mathbf{r}, \tau) d\tau, \tag{5.1}$$

where γ is the gyromagnetic ratio of the nucleus. The signal σ received from the imaging volume V reads

$$\sigma(t) = \int_V \rho(\mathbf{r}) e^{i\phi(\mathbf{r},t)} d\mathbf{r}, \tag{5.2}$$

with $\rho(\mathbf{r})$ being the initial transverse magnetization, $\phi(\mathbf{r}, t)$ being the phase of the magnetization and $i = \sqrt{-1}$. Conceptually, the field evolution can be separated into *dynamic* field components (primarily generated by the scanners' gradient system), and *static* field components as determined by the main magnetic field and susceptibility induced field components of potentially very high spatial order. Commonly the *dynamic* field components are assumed to be strictly linear in space and are typically written as $\mathbf{r} \cdot \mathbf{k}(t)$, where $\mathbf{k}$ is the time integral of a linear gradient times γ. In the presence of non-linear fields the conventional k-space formalism is insufficient to describe the phase evolution. To incorporate higher-order *dynamic* contributions we employ a more general model: the phase evolution is expanded into a set of higher-order spatial basis functions. This approach is motivated by the fact, that the sources of the dynamic fields are relatively far away from the imaging object, such that the field distribution is of relatively low spatial order and can be captured by a relatively small basis set. Adopted from magnetostatics where $\mathbf{B}$ satisfies the Laplace equation, solid harmonics [97] (spherical harmonics) provide a natural choice of basis functions. Additionally the *static* field components can be integrated [98] by the phase term created by the static field off-resonance. A phase model comprising static and dynamic components reads [72]

$$\phi(t, \mathbf{r}) = \sum_{l,m} \left(k_l^m(t) Y_l^m(\mathbf{r})\right) + \gamma B_{ref}(\mathbf{r}) t, \tag{5.3}$$

where Y_l^m is the spherical harmonic function of degree l and order[†], $m k_l^m$ is the phase coefficient corresponding to that function and $B_{ref}(\mathbf{r})$ describes the static main field $B_0(\mathbf{r})$ at the reference time point. Real-valued solid harmonics (or spherical harmonics) listed up to degree $l = 3$ are given in table 5.2.4.

To determine the phase coefficients $k_l^m(t)$, the phase evolution is measured by field probes in a number of well defined positions around the imaging volume. The phase coefficients are then retrieved by fitting the measured phase data to the chosen set of basis functions [72]. Note that favorably the phase evolution is measured during the imaging experiment, or instead in a separate calibration experiment.

The incorporation of static off-resonances in the image reconstruction requires a B_0 map which is typically obtained from two scans with different

---

[†] Note that for spherical harmonic functions the word *order* relates to its zonal, sectorial or tesseral behavior. Throughout this text the word order is used as the highest degree of the employed basis function set.

echo times [99]. Alternatively, $B_{ref}(\mathbf{r})$ is set to B_0 as delivered by the center frequency determination.

5.2.2 Image reconstruction as an inverse problem

The signal encoding Eq. (5.2) is continuous in both the temporal and the spatial domain. In an MRI experiment the time domain is inherently discretized by data sampling. When also discretizing the spatial domain (to an arbitrarily fine degree), Eq. (5.2) can be written in matrix-vector form

$$E\boldsymbol{\rho} + \boldsymbol{\eta} = \boldsymbol{\sigma}. \tag{5.4}$$

Here $\boldsymbol{\rho}$ is the column vector containing the magnetization in the image domain, $\boldsymbol{\eta}$ is the corresponding noise vector, $\boldsymbol{\sigma}$ is the acquired signal vector and E is a matrix containing the encoding terms, i.e. the encoding matrix, for each discretized point in time and space

$$E_{\kappa,\lambda} = e^{i\phi(t_\kappa,\mathbf{r}_\lambda)}, \tag{5.5}$$

where κ, λ count the sampling time points and pixels of the target image, respectively. Using the phase model as given in Eq. (5.3), E reads

$$E_{\kappa,\lambda} = e^{i\sum_{l,m} k_l^m(t_\kappa)Y_l^m(\mathbf{r}_\lambda)+\gamma B_{ref}(\mathbf{r}_\lambda)t_\kappa}. \tag{5.6}$$

Image reconstruction can be performed by viewing eq. (5.4) as an inverse problem [96]. One apporach is to minimize the weighted sum of the remaining image artefact and the (reconstructed) noise power. The ensuing reconstruction matrix was proposed previously [100] and the reconstructed image is given by

$$\boldsymbol{\rho} = (E^H\tilde{\Psi}^+E + \alpha\Theta^+)^+E^H\tilde{\Psi}^+\boldsymbol{\sigma}, \tag{5.7}$$

$$\boldsymbol{\rho} = E^+\boldsymbol{\sigma} \tag{5.8}$$

$$\phi(t,\mathbf{r}) = (k^x(t) + k^y(t) + k^z(t) + Y_l^m(\mathbf{r})) + \gamma B_{ref}(\mathbf{r})t, \tag{5.9}$$

where $\tilde{\Psi}$ denotes the sample noise matrix [96], which describes the levels and the correlation of stochastic noise in signal samples, and Θ describes the spatial signal correlation in the image pixels [100]. With the

integration of $\tilde{\Psi}$ and Θ, the scalar factor α allows for a weighting preference of minimizing noise and spatial response function (SRF) deviation respectively in the image to be reconstructed. In single coil reconstruction $\tilde{\Psi}$ is given as a scalar c_1 (the expected noise level) times identity I, and by integration of c_1 into α may be omitted from eq. (5.7). Similarly, without prior knowledge in the spatial domain the signal values are assumed to be uncorrelated. In this case the signal covariance Θ is given by the unknown expected mean signal c_2 times identity I. Hence, by keeping the weighting fact α, Θ^+ can be replaced by identity I.
For $E^H E$ to be invertible, E must have more columns than rows (i.e. $\boldsymbol{\sigma}$ has more samples than $\boldsymbol{\rho}$ pixels), which is no longer the case if the spatial domain is discretized on an arbitrarily fine grid to reconstruct on higher resolution. A small α can be chosen to ensure positive definiteness of the matrix while still focusing on correct depiction of the image. In this case the reconstruction reduces to a Tikhonov regularized solution:

$$\boldsymbol{\rho} = (E^H E + \alpha I)^+ E^H \boldsymbol{\sigma}. \tag{5.10}$$

5.2.3 Spatial variation of the encoding characteristics

Due to the spatial non-linearity of the dynamic fields, spatial encoding varies over the imaging volume. Particularly in off-center regions, where the dynamic higher-order effects become relatively strong, the local gradient may deviate considerably from the nominally applied gradient. To characterize aberrations of spatial encoding in the conventional k-space picture, the concept of local k-space is used [101]. In accordance to the common k-space formalism, $\mathbf{k}_{local}$ is defined via the local derivative of B (i.e. the gradient) in each location $\mathbf{r}$:

$$\mathbf{k}_{local}(\mathbf{r}, t) = \gamma \int_0^t \nabla B(\mathbf{r}, \tau) d\tau = \int_0^t \nabla \phi(\mathbf{r}, \tau) d\tau. \tag{5.11}$$

In the image domain higher-order effects can be displayed by looking at the SRF. In an image reconstructed on the basis of eq. (5.10), the spatial response function (SRF) of each point in space is given by

$$SRF_\lambda(\mathbf{r}) = \sum [(E^H E + \alpha I)^+ E^H]_{\lambda,\lambda} \cdot e^{i\phi(t_\kappa, \mathbf{r})}, \tag{5.12}$$

showing the spatial weighting of signal sources in the object assigned to voxel λ. Similarly the spatial encoding may be assessed by the point spread function (PSF) which can be obtained using the same equation being evaluated as a function of λ, while fixing the source signal position $\mathbf{r}$ to the position of a voxel-center of interest.

5.2.4 Iterative higher-order reconstruction

Solving Eq. (5.10) involves the handling of large matrices. The encoding matrix E is of size $N_\kappa \times N_\lambda$, where N_λ and N_κ denote the number of pixels and the number of signal samples respectively. Direct computation of the pseudo-inverse of $E^H E + \alpha I$ calls for a matrix matrix multiplication $E^H E$ of complexity $\mathcal{O}(N_\lambda^2 N_\kappa)$ (Landau notation [102]) as well as the inversion of $E^H E + \alpha I$ using Gauss elimination ($\mathcal{O}(N_\lambda^3)$). Therefore computation times get unpractical for typical image matrix sizes. Instead, iterative solvers such as the Jacobi method, the Gauss-Seidel method or the conjugate-gradient method can be employed to achieve adequate reconstruction times. With these methods a solution $\tilde{\boldsymbol{\rho}}$ to the linear system $(E^H E + \alpha I)\boldsymbol{\rho} = E^H \boldsymbol{\sigma}$ is iteratively approximated until a sufficiently accurate solution is found. Among iterative solvers the conjugate gradient method has the advantage of achieving fast convergence and low memory consumption and therefore became popular in MR image reconstruction [96]. For the conjugate gradient method the complexity of each iteration step is governed by multiplications of E or E^H with a vector ($\mathcal{O}(N_\lambda N_\kappa)$). Unlike in Fourier encoding and reconstruction (that is also utilized in gridding [103] based reconstruction techniques), the mentioned multiplications can not be accelerated by the use of fast Fourier transforms (FFTs). Due to the general form of the encoding term (Eq. (5.6)), the matrix vector multiplications have to be calculated explicitly. In order to do so the values of E may either be pre-calculated and stored in fast accessible memory, or have to be calculated on demand, the latter being especially beneficial for larger imaging matrices. Note that using this reconstruction formalism, incorporating static B_0 correction only requires marginally longer reconstruction times. Pseudocode describing the used conjugate gradient method as well as the involved calculation and multiplication of E and E^H with vector data is given in appendix A.

degree l	order m	function
0	0	1
1	-1	x
	0	z
	1	y
2	-2	xy
	-1	zy
	0	$3z^2 - (x^2 + y^2 + z^2)$
	1	xz
	2	$x^2 - y^2$
3	-3	$3yx^2 - y^3$
	-2	xyz
	-1	$(5z^2 - (x^2 + y^2 + z^2))y$
	0	$5z^3 - 3z(x^2 + y^2 + z^2)$
	1	$(5z^2 - (x^2 + y^2 + z^2))x$
	2	$x^2z - y^2z$
	3	$x^3 - 3xy^2$

Table 5.1: Solid Spherical Harmonics up to the 3^{rd} order omitting constant factors

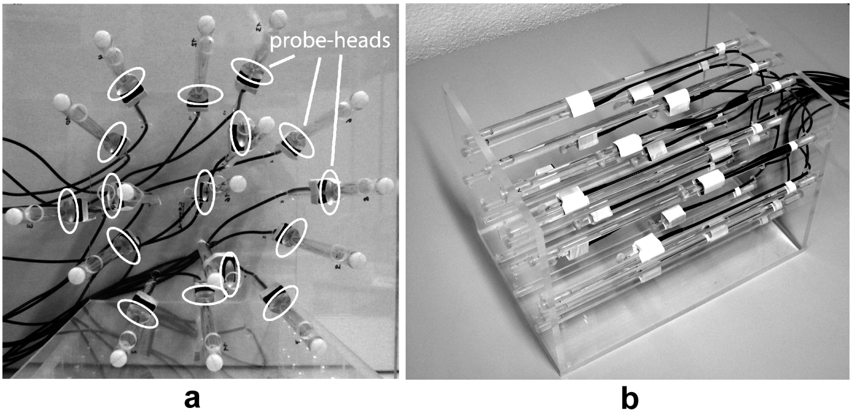

Figure 5.1: Field Camera with the 16 NMR probes. Front view (a) and side view (b). To measure the field evolution during an MR sequence the gantry is placed in the magnet bore and connected to the scanner system.

5.2.5 Hardware and phantoms

Imaging data was acquired on a 3T Philips Achieva MR scanner using an 8-channel head receiver array (Philips Healthcare, Best, The Netherlands). The phase evolution was acquired using a higher order dynamic field camera [95] consisting of 16 NMR probes (H_2O doped with $CuSO_4$, 0.7 mm droplet diameter, 3-turn solenoid, wire diameter 71 μm, $SNR\sqrt{BW} = 4.8 \cdot 10^4 \sqrt{Hz}$, non-RF-shielded) [94], equally distributed on a 20 cm sphere (Fig. 5.1). The NMR probes were operated in transmit/receive (T/R) mode and excited simultaneously by a 4.5 μs RF pulses generated by a separate transmit chain [94]. The resulting NMR signals are received via T/R switches with integrated preamplifiers and fed into 16 regular channels of the system spectrometer. The miniaturized probe droplets tolerate gradient action up to $k_{max} = 9000\ rad/m$, corresponding to a resolution of 350 μm before dephasing. Their signal lifetime is 150 ms, capturing field evolutions up to this duration with a single excitation.

To facilitate data analysis a spherical phantom filled with low-diffusive silicon oil (AK 350, Wacker Chemie AG, Munich, Germany) was employed for the in-vitro scans, such that high image SNR is achieved also in the diffusion weighted data.

5.2.6 Data Acquisition

Data acquisition was performed in two steps. Firstly imaging scans were performed using the spherical phantom and in healthy human brain respectively. 2D single-shot echo-planar (EPI) spin-echo data (TR = 5000 ms, TE = 84 ms, 76 phase encodes, readout duration = 45.8 ms, FOV = 230 mm) was acquired in a coronal (in-vitro) and a transverse (in-vivo) plane. Diffusion weighting ($b = 1000\ s/mm^2$) was applied in the frequency-encoding (DW_f), phase-encoding (DW_p) and slice-selection direction (DW_s) (Fig.5.2(a)). Along with the DW images minimally diffusion weighted (b_0) images were acquired. To obtain a B_0 map, two spin-warp gradient echo images (TE = 2.4 ms / 3.0 ms, TR = 300 ms, 116 phase-encodes) of the same slice and FOV were acquired. The (DW) EPI scans were repeated using the DW-single-shot EPI protocol of the system, with all scan parameters chosen as close as possible to those mentioned above.
In a second step both, the imaging object and the head coil, were removed from the scanner and replaced by the field camera. Subsequently all imaging experiments were repeated to acquire phase data from the 16 NMR probes. In the DW experiments the probes were simultaneously excited after the second diffusion gradient, Fig.5.2(a). In the gradient echo experiments the probes were excited right after the slice selection gradient, Fig.5.2(b).

5.2.7 Image reconstruction

The phase coefficients k_l^m were obtained by least-square fitting of the NMR-probes phase data to a full 3^{rd} order solid harmonics basis set (Table 5.2.4) for each scan. Throughout this text this phase model is referred to as the 3^{rd} *order phase model* and reconstructions using the ensuing k_l^m's are termed *higher-order reconstructions*. For comparison so called 1^{st} *order phase models* are derived from the 3^{rd} order phase models by omitting 2^{nd} and 3^{rd} order phase coefficients.

From the two gradient echo images a phase map ω_{B_0} was calculated and served as an input for static off-resonance correction of the EPI images using the higher-order reconstruction. Subsequently the diffusion-weighted EPI datasets were reconstructed with and without static B_0 correction using the higher-order field model as well as the 1^{st} order phase model. Another set of images was reconstructed by using the nominal (1^{st} order)

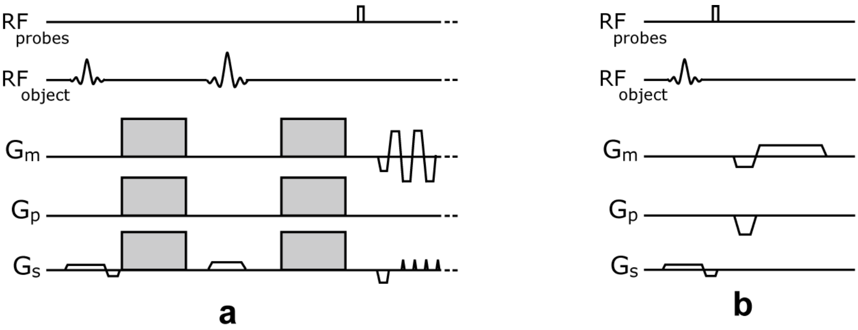

Figure 5.2: Schematic sequence diagrams: (a) Standard Stejskal-Tanner sequence with the refocusing pulse between the diffusion sensitizing gradients (gray). The NMR probes are excited after the second diffusion gradient lobe followed by the echo planar readout. (b) Gradient echo sequence with NMR probes excited after the slice selection rewinder gradient

EPI trajectory, termed *nominal reconstruction*. The datasets acquired with the standard scanner DWI acquisition method were reconstructed using the standard scanner reconstruction. From these images another set of images was obtained by coregistering [26] b_0 and DW to the mean image of the three DW images.

The iteration of the conjugate gradient solver was aborted after obtaining visually satisfying results. The data from each coil element was reconstructed separately and the final image was calculated as the root of sum of squares of each single-channel image. To avoid excessive memory demand of the reconstruction, the values of E were calculated on demand for their multiplication with vector data. The matrix vector multiplications were distributed to an AMD Opteron cluster with 32 independent CPUs such that the computation time for one conjugate gradient iteration amounted to approximately 3 seconds for a single-channel EPI image.

5.3 Results

5.3.1 Higher-order field terms

The unit of each phase coefficients k_l^m depends on the degree l of the corresponding basis function and is given as rad/m^l. As mentioned previously, the effect on the phase $k_l^m Y_l^m(\mathbf{r})$ varies withing the imaging volume V (i.e. a sphere with 20 cm diameter). To get a feeling for their relative importance, the maximum phase contribution in rad within the imaging volume $(max(\phi_l^m(t)) = k_l^m(t) \cdot max_V(Y_l^m(\mathbf{r})))$ can be depicted as done in Fig. 5.3.
The phase evolution during the non-DW EPI is shown in Fig. 5.3(a). As expected the dynamic field-evolution is dominated by the 1^{st} order frequency and phase encoding gradients relating to the phase coefficients k_1^{-1} and k_1^1. Only one higer-order phase coefficient (k_2^0) perceptibly contributes to the phase evolution of the scan (Fig. 5.3(a)). The accumulating 0^{th}-order phase (sometimes called the B_0-phase) indicates a slight misdetermination of center-frequency by the system. To reveal the effect of diffusion-weighting on the field, the difference in phase evolution between the DW and non-DW (b_0) acquisitions is plotted (Fig. 5.3(b,c,d)). For these scans considerable higher-order fields effects are apparent. These field contributions are likely related to long-term eddy currents induced in various conducting strucutres of the scanner system including the gradient coils themselves. The fact that higher-order induced effects exceeded the linear eddy current induced effects in some parts of the (even relatively small) FOV (Fig. 5.5(b-d)) is attributed to a good eddy current compensation of the system that compensates well for 0th-order and 1^{st} order fields, but is unable to compensate for higher-order field perturbations.

5.3.2 Depiction characteristics

To assess spatial dependence of spatial encoding in the classical k-space picture, local k-space trajectories $\mathbf{k}_{local}(\mathbf{r})$ are obtained by eq.(5.11) using the full 3^{rd} order field model. For the EPI trajectory with DW applied in frequency-encoding direction as shown in Fig. 5.3(a, b), $\mathbf{k}_{local}(\mathbf{r})$ is computed for each pixel center within the FOV. For comparison a k-space trajectory $\mathbf{k}_{global}(\mathbf{r})$ is obtained from eq.(5.11) using the 1^{st} order field model. Static B_0 inhomogeneity is omitted in the evaluation of $\mathbf{k}_{local}(\mathbf{r})$ [34]. Maps showing the maximum difference $\delta\mathbf{k}^{x,y}$ between $\mathbf{k}_{local}^{x,y}(\mathbf{r}) - \mathbf{k}_{global}^{x,y}$ over the

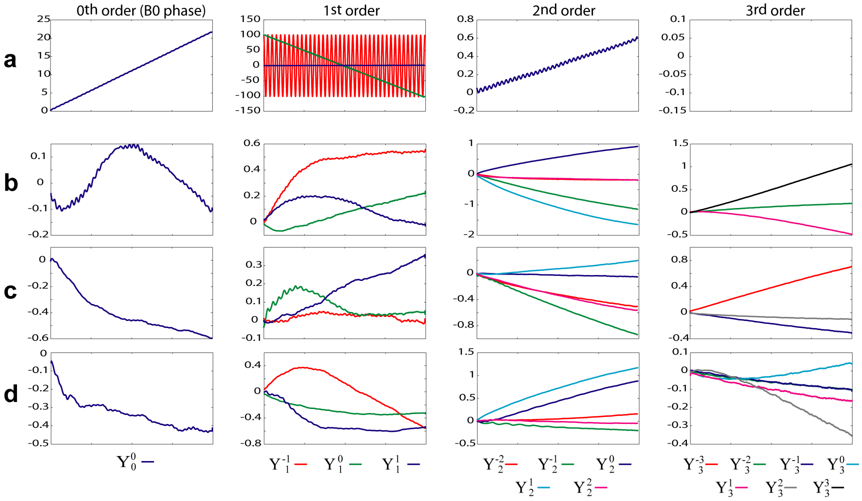

Figure 5.3: Phase evolution (maximum phase contribution within the imaging volume in *rad*) over the time of the readout (45.8 ms) of a single-shot EPI scan (a) separately plotted for each phase coefficient k_l^m grouped by the degree of the spherical harmonic basis functions. Diffusion weighting induced field components for DW in frequency encoding direction (b), DW in phase encoding direction (c) and DW in slice direction (d). Phase coefficients with a maximum phase accrual of less than 0.1 rad within the FOV are omitted in the plots.

time of the readout in frequency encoding (x) and phase encoding (y) [888 rename x y -¿ f p?]direction are calculated for each pixel. A strong variation is observed (Fig. 5.4(a,b)) within the FOV, the off-center regions being particularly effected. The local k-space trajectory deviated by up to ±100 rad/m in the phase-encoding direction (Fig. 5.4(a)), which for the given resolution and matrix size corresponds to more than three times the fold Nyquist sampling distance. In the frequency encoding direction the maximum deviation ranges from -40 to 80 rad/m (Fig. 5.4(b)). The local k-space is investigated in detail for two sample pixels λ_1 (off-center coordinate $(0.112\,m, 0m, -0.085\,m)$) and λ_2 $(0.112\,m, 0\,m, 0.067\,m)$ (Fig. 5.4(a,b)). In these pixels the maximum difference δk is 62 rad/m (λ_1) and -63 rad/m (λ_2) in the phase direction, and -16 rad/m (λ_1) and -14 rad/m (λ_2) in the frequency encoding direction. This is also visible in the k-space trajectory of these pixel, where $\mathbf{k}^{x,y}_{local}(\mathbf{r})$ (Fig. 5.4(d,e)) shows a cumulated deviation from $\mathbf{k}^{x,y}_{global}(\mathbf{r})$ (Fig. 5.4(c)) that is primarily visible in the phase encoding direction.

To assess the effects of higher-order field components in the image domain, SRFs are calculated according to eq. (5.12) for the same acquisition and the pixels λ_1 and λ_2. The signal point sources $e^{i\phi(t_\kappa,\mathbf{r})}$ (eq. (5.12)) at each position r are generated using the measured full 3^{rd} order phase model. To asses the benefit of the higher-order reconstruction, a *higher-order SRF* is calculated using the full 3^{rd} order encoding matrix (Fig. 5.5 (solid line)) and a 1^{st} *order SRF*, assuming the 1^{st} order phase model (Fig. 5.5 (dashed line)). To fully resolve spatial variation in terms of resolution, the image matrix is set to twice of its nominal size. The difference in the local k-space trajectory (Fig. 5.4) also is manifested in their spatial response: For λ_2 a higher resolution in terms of full width at half maximum (FWHM) is achieved than in λ_1 (Fig. 5.5(a)). As a result of neglecting higher-order effects during image reconstruction, misinterpretation of the acquired signal leads to signal contributions from neighboring voxel centers and spatial shifts of the SRF (Fig. 5.5(a)). The same effect is visible when looking at the PSFs (Fig. 5.5(b)) where smearing and shifts of the PSF is apparent for the 1^{st} order reconstructions, while the higher-order PSF shows an unshifted sinc-like shape.

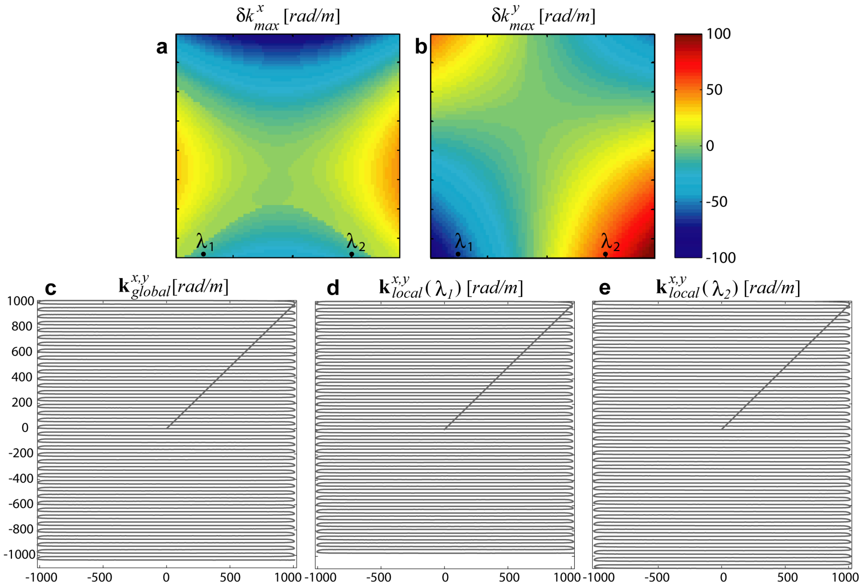

Figure 5.4: Effects of the higher-order fields for a single-shot EPI scan with DW in frequency encoding direction: Differences δk between local and global k-space trajectory in phase-encoding (a) and frequency-encoding direction (b) for all pixels within the FOV. Local k-space trajectory for pixel λ_1(d) and λ_2(e) in the presence of higher-order fields and the global k-space trajectory obtained by neglecting higher-order effects (c)

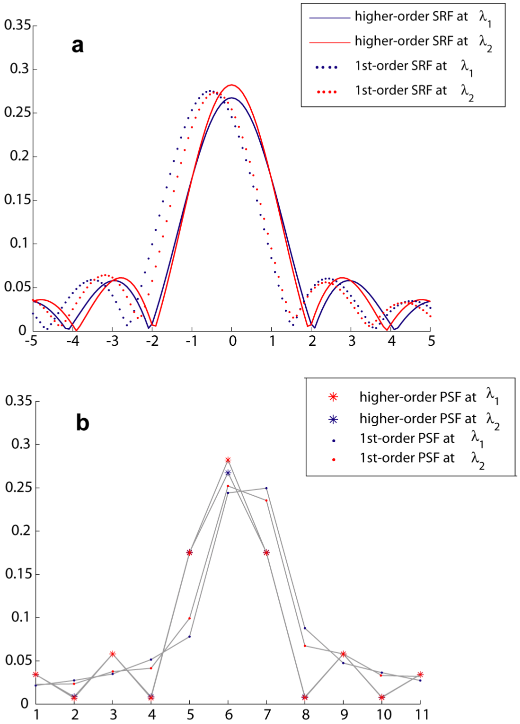

Figure 5.5: ((a): Spatial response functions of pixels λ_1 (blue) and λ_2 (red) for an EPI readout with DW in frequency-encoding direction: 1^{st} order (dashed line) and higher-order (solid line) reconstruction. (b) Point spread function (PSF) for the same readout using the higher-order (*) and the 1^{st} order reconstruction ($\cdot$).

5.3.3 Geometrical congruence of diffusion weighted images

To assess the geometrical inconsistency of the variably diffusion encoded images, absolute difference images between in-vitro DW images and the b_0 image were produced for a number of image sets: standard acquisition/reconstruction (w/wo image coregistration [26]), nominal reconstruction, measured 1^{st} order reconstruction (w/wo B_0 correction) and full 3^{rd} order reconstruction (w/wo B_0 correction).

To separate the effect of geometrical congruence from difference in magnitude caused by the diffusion weighting, all images were normalized to a mean value of 1 within the phantom.

Congruence within each dataset is indicated by two measures ($\epsilon_{max}, \epsilon_{mean}$), the maximum and mean values in the difference images. They vary drastically between the different reconstruction strategies (Fig. 5.7). Elevated difference values are apparent in all 1^{st} order based reconstructions (Fig. 5.7(a-d,f)). Among the 1^{st} order based reconstruction standard reconstruction (Fig. 5.7(a)) and reconstruction on the nominal trajectory (Fig. 5.7(c)) resulted in the least congruent images with $\epsilon_{max}(b_0 - DW_s) = 0.67$ and $\epsilon_{max}(b_0 - DW_s) = 0.61$ respectively. Based on affine-transformations the coregistration of the standard reconstructed images improved image congruence only slightly (Fig. 5.7(b)) ($\epsilon_{max}(b_0 - DW_s) = 0.41$). The reconstructions based on the measured 1^{st} order field model (taking into account the $0^{th}-$ and 1^{st} order eddy current induced terms) reduced the errors compared to the standard reconstruction. However only the incorporation of higher-order terms substantially improved image congruence (Fig. 5.7(e,g)) with differences $\epsilon_{max} = 0.04$, 0.05 and 0.25 between b_0 image and three DW images. This finding also indicates that the 3^{rd} order field model is largely sufficient to describe the dynamic field evolution in these experiments.

Static off-resonance correction was applied to the 1^{st}- and 3^{rd} order field models employing the measured B_0 map (Fig. 5.6) generated from the gradient echo images. The resulting images display the actual round shape of the object while achieving similar image congruence (Fig. 5.7(f,g)) as with the non-B_0 corrected reconstructions (Fig. 5.7(d,e)). Note that for the images reconstructed on the basis of the measured field evolution (Fig. 5.7(d-g)) no phase correction needed to be applied as opposed to conventional EPI imaging (Fig. 5.7(a,b)). Reconstruction based on the actual phase evolution inherently avoids n/2 ghosting artifacts as observed in the im-

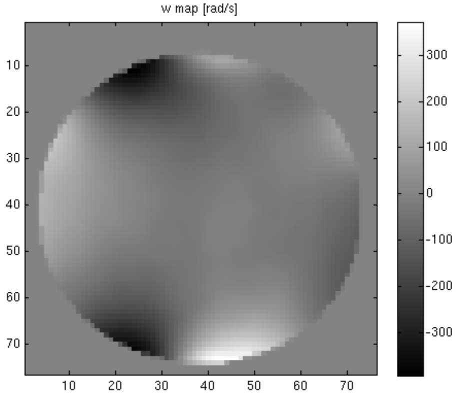

Figure 5.6: Static off-resonance frequency map ω_{B_0} of the spherical phantom [rad/s], measured by the spin-warp gradient echo imaging with TE $= 2.4$ *ms* and 3.0 *ms*

ages reconstructed with the nominal trajectory (Fig. 5.7(c)).

The in-vivo data was reconstructed using the 3^{rd} order field model (Fig. 5.8). Neither n/2 Ghosting artifacts nor distortions are visible in the b_0 image (Fig.5.8(a)) and the DW images (Fig.5.8(b-d)) Fig.5.8(e)). Hence, image fusion was possible without loss in resolution which can be seen in the mean diffusion weighted image and in the apparent diffusion coefficient (ADC) map derived from these images (Fig.5.8(f)). This confirms the finding from the in-vitro analysis where excellent image congruence is achieved.

5.4 Discussion and Conclusion

The present work introduces a method to incorporate higher-order dynamic field terms into image reconstruction. Accurate field measurements were obtained by a field camera based on NMR probes. It was shown that non-linear fields can have a considerable effect on the spatial encoding. The impact of non-linear fields was analyzed in the common k-space formalism and in the spatial domain for the example of a diffusion-weighted image acquisition. Investigations showed that neglecting higher-order field terms

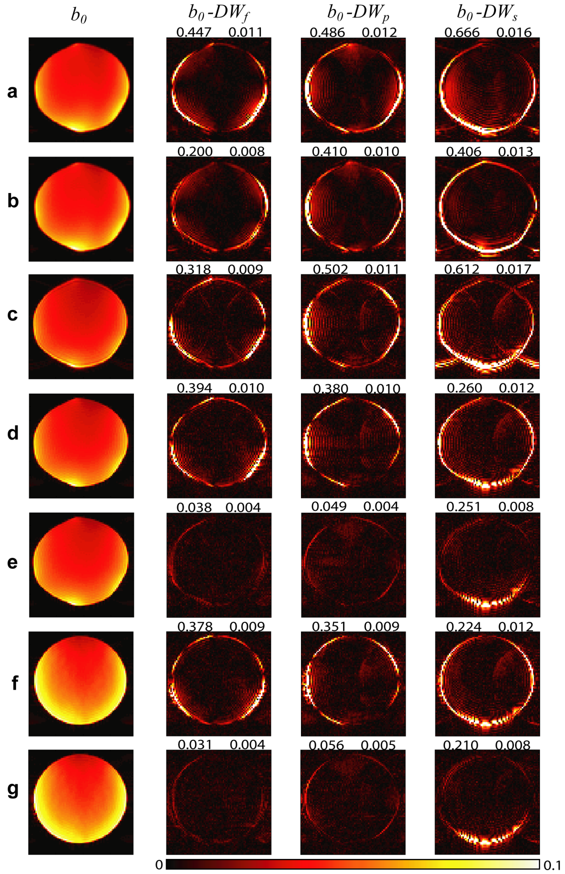

Figure 5.7: Assesment of image congruence by difference images between a non-DW (b_0) image (left) and the diffusion-weighted (frequency, phase and slice direction) images: standard reconstruction on the scanner system (a), standard reconstruction on the scanner system and subsequent image-coregistration (b), reconstruction assuming the nominally applied (1^{st} order) EPI trajectory (c), 1^{st} order reconstruction based on measured data with (e) and without (d) static off-resonance correction, higher-order reconstruction based on measured data with (g) and without (f) static off-resonance correction. Maximum ϵ_{max} and mean ϵ_{mean} values are displayer above each image.

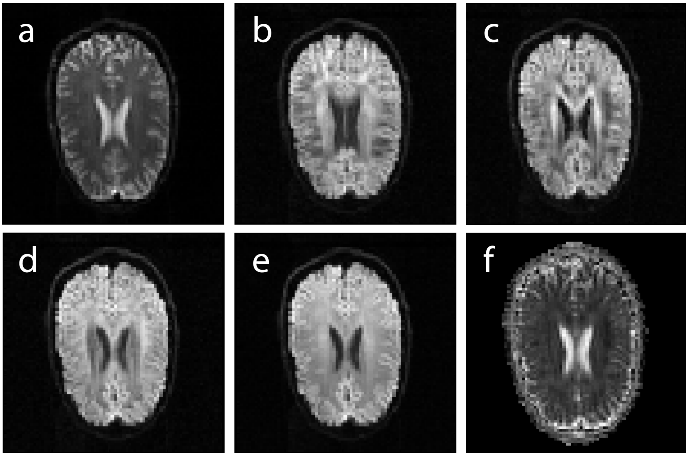

Figure 5.8: In-vivo single-shot EPI: (a) non-DW (b_0) image, (b) DW in frequency encoding direction, (c) DW in phase encoding direction, (d) DW in slice encoding direction, (e) mean DW image and (f) apparent diffusion coefficient (ADC) map

leads to shifts and broadening of the SRFs. This result was confirmed by a phantom study, where the incorporation of measured higher-order dynamic fields solved the problem of geometrical inconsistency for variably diffusion encoded single-shot EPI data.

The effect of unaccounted (higher-order dynamic) fields on the SRF is emphasized in long aquisitions. By integration of these terms, the presented reconstruction algorithm renders possible to prolong readout durations. In various MRI applications it is desirable to increase SNR efficacy as well as to improve motion-insensitive single-shot imaging. Thereby the presented technique can directly improve quantitative MRI methods such as fMRI, DTI or magnetization transfer imaging where single-shot imaging is highly favorable.
Furthermore the achieved geometrical congruence serves as the basis for accurate static B_0 correction which is imperative for longer acquisition durations, and could be particularly useful when aiming at non-Cartesian acquisition. Conversely the correction of higher-order dynamic fields dur-

ing image reconstruction can reduce the demands on the linearity of the dynamic field behavior, and thereby may ultimately reduce the cost of MR systems.

In the present study dynamic fields were modeled by a spatial expansion into a full set of spherical harmonic basis functions up to the 3^{rd} order based on measured data. Static inhomogeneities were integrated using a B_0 map. However, the provided reconstruction algorithm constitutes a platform that is open for other phase models. For example the presented algorithm is amenable to an even higher order basis set. Other phase models could also include physiologically induced dynamic susceptibility changes. The presented reconstruction algorithm can be extended to partial Fourier encoded acquisition or parallel imaging. Another application is the combination of higher-order reconstruction based on monitored field data with dynamic shimming [104], where slow time constants and imperfections of the (higher order) shim system could be corrected at the reconstruction stage.

As shown in the SRF study, higher-order field terms result in locally varying image resolution. To fully benefit from the available resolution, image reconstruction must be performed on a finer grid, or even on non-equidistantly spaced points. Here, local k-space evaluations may serve as an input for the choice of spatial discretization. In this context the Tikhonov regularization provides a simple and useful tool to guarantee convergence of the reconstruction algorithm for underdetermined problems.
Higher order fields also result in local violation of the Nyquist criterion. Unlike the resolution, the spatial discretization in terms of FOV cannot be considered locally. In the investigated experiments, the FOV was set to its nominal value without the occurrence of aliasing artifacts. However, in case of stronger higher-order fields [105] a more conservative planning of the FOV is required. Alternatively artifacts due to encoding deficiencies can be drastically reduced by the incorporation of B_1 sensitivity encoding into image reconstruction.

As compared to Fourier based reconstructions, the presented approach is computationally demanding. For the presented 2D imaging experiments reconstruction times were in the range of a few minutes. Image reconstruction might be accelerated by algorithms that suitably interpolate static and dynamic field terms (similar to multi-frequency-interpolation [106]). On the other hand optimized implementations, faster CPUs or implementations on vector computing architectures [107] may enable a speedup of several orders of magnitude without compromising accuracy and simplicity of the presented approach.

5.5 Appendix

Algorithm *IterativeImageReconstruction*
Input: time signal vector $\boldsymbol{\sigma}$
Output: approximate image solution vector $\tilde{\boldsymbol{\rho}}$
(∗ Higher-order reconstruction using the conjugate gradient approach ∗)

```
$\tilde{\boldsymbol{\rho}} \leftarrow 0$
$\mathbf{p} \leftarrow E^H(\boldsymbol{\sigma})$
$\boldsymbol{\delta} \leftarrow \mathbf{p}$
while not converged
        $\mathbf{q} \leftarrow E^H(E(\mathbf{p})) + \alpha\mathbf{p}$
        $\tilde{\boldsymbol{\rho}} \leftarrow \tilde{\boldsymbol{\rho}} + \frac{\boldsymbol{\delta}^H\boldsymbol{\delta}}{\mathbf{p}^H\mathbf{q}}\mathbf{p}$
        $\boldsymbol{\delta}_{old} \leftarrow \boldsymbol{\delta}$
        $\boldsymbol{\delta} \leftarrow \boldsymbol{\delta} + \frac{\boldsymbol{\delta}^H\boldsymbol{\delta}}{\mathbf{p}^H\mathbf{q}}\mathbf{q}$
        $\mathbf{p} \leftarrow \boldsymbol{\delta} + \frac{\boldsymbol{\delta}^H\boldsymbol{\delta}}{\boldsymbol{\delta}_{old}^H\boldsymbol{\delta}_{old}}\mathbf{p}$
return $\tilde{\boldsymbol{\rho}}$
```

Algorithm $E(v)$
Input: $\mathbf{v}$ $(N_\lambda \times 1)$, time $\mathbf{t}$ $(N_\kappa \times 1)$, $\mathbf{k}_l^m$ $(N_\kappa \times 1)$, $\omega_{\delta B_0}$
Output: time domain vector $\mathbf{u}$ $(N_\kappa \times 1)$
(∗ Calculation E and multiplication of with a vector $\mathbf{v}$ ∗)

```
$\mathbf{u} \leftarrow \mathbf{0}$
for $\lambda \leftarrow 1$ to $N_\lambda$
        $\boldsymbol{\phi} \leftarrow \mathbf{0}$
        for all $l, m$
                $\boldsymbol{\phi} \leftarrow \boldsymbol{\phi} + \mathbf{k}_l^m Y_l^m(\mathbf{r}_\lambda)$
        if staticB0Correction
                $\boldsymbol{\phi} \leftarrow \boldsymbol{\phi} + \omega_{\delta B_0}(\mathbf{r})\mathbf{t}$
        $\mathbf{u} \leftarrow \mathbf{u} + (e^{i\boldsymbol{\phi})})\mathbf{v}_\lambda$
return $\mathbf{u}$
```

Algorithm $E^H(u)$
Input: $\mathbf{u}$ $(N_\kappa \times 1)$, time $\mathbf{t}$ $(N_\kappa \times 1)$, $\mathbf{k}_l^m$ $(N_\kappa \times 1)$, $\omega_{\delta B_0}$
Output: image domain vector $\mathbf{v}$ $(N_\lambda \times 1)$
(∗ Calculation of E^H and multiplication with a vector $\mathbf{u}$. ∗)

```
$\mathbf{v} \leftarrow \mathbf{0}$
for $\lambda \leftarrow 1$ to $N_\lambda$
        $\boldsymbol{\phi} \leftarrow \mathbf{0}$
```

```
    for all $l, m$
        $\boldsymbol{\phi} \leftarrow \boldsymbol{\phi} + \mathbf{k}_l^m Y_l^m(\mathbf{r}_\lambda)$
    if staticB0Correction
        $\boldsymbol{\phi} \leftarrow \boldsymbol{\phi} + \omega_{\delta B_0}(\mathbf{r}_\lambda)\mathbf{t}$
    $\mathbf{v}_\lambda \leftarrow (e^{i\boldsymbol{\phi}})^H \mathbf{u}$
return v
```

Chapter 6

Conclusion and Outlook

The reduced FOV approach described in chapter 2 and 3 has proved to be enormously beneficial for DWI and DTI acquisition by improving SNR efficiency and image quality at the same time. The technique is applicable for imaging of objects being geometrically limited in at least one dimension, and may also be employed for non-DW MRI where single-shot imaging is necessary. In the spinal cord, this technique enabled the acquisition of DW images with sub-millimeter resolution at all levels of the spinal cord for the first time. In particular the obtained images allow for separation of gray matter and white matter, thereby potentially increasing specificity and sensitivity of the derived quantitative measures. The technique is currently being employed in three ongoing clinical studies: One being dedicated to the assessment of white matter changes in the different types of spinal cord multiple sclerosis [108], a second study to assess Wallerian degeneration in tetraplegic patients following spinal cord injury, and the third study is investigating the feasibility of the detection of prostate carcinoma using DTI [109]. Further improvements for spinal cord DWI should focus on the investigation of patient motion induced field variation which could render the use of dynamic shimming approaches interesting. Additionally improved coil design for spinal cord imaging could further increase SNR and thereby image quality. Optimized coils could also render acquisition at even higher field strength (7T) very promising.

The problem of eddy-currents induced by the strong diffusion-weighting gradients was solved on a general level by magnetic field monitoring. The developed transmit/receive system described in chapter 4 enabled independent and robust excitation of the NMR field probes at any time of the sequence, which is essential for concurrent field monitoring in DWI. Robust excitation of the probes was also a necessary step for the development of the field camera using 16 NMR probes that is described in chapter 5. The field camera measurements showed that DW induced eddy currents have considerable higher-order components. In particular the higher-order field effects exceed the linear field deviations in off-center regions of the scanner, such that it is not surprising that previous approaches neglecting these fields do not succeed in achieving good congruence among variable b value DW images. The algorithm that was developed to integrate the measured high-order dynamic field contributions substantially corrects all eddy-current distortions, thereby providing the basis for high-resolution DTI or q-space methods with improved accuracy.

The benefit of higher-order field monitoring was shown for the example of DWI. However, the technique may be applied in many other situations where imperfections of the predescribed field evolution limit quality or feasibility of an MR experiment. A topic for future research might be the integration of the field probes into imaging coils. Thereby concurrent field-monitoring could be employed on a regular basis also in clinical settings, ultimately also improving the attainable resolution in spinal cord DWI.

References

[1] S Skare. *Optimisation Strategies in Diffusion Tensor MR Imaging.* MR Center, Dept. of Clinical Neuroscience Karolinska Institutet, Stockholm, Sweden, 2002.

[2] R. Bammer. Basic principles of diffusion-weighted imaging. *Eur J Radiol*, 45:169–184, Mar 2003.

[3] T. A. Huisman, H. Hawighorst, C. H. Benoit, and A. G. Sorensen. [Diffusion weighted MRI: ischemic and traumatic injuries of the central nervous system]. *Radiologe*, 41:1038–1047, Dec 2001.

[4] P. W. Schaefer. Applications of DWI in clinical neurology. *J. Neurol. Sci.*, 186 Suppl 1:25–35, May 2001.

[5] D. Le Bihan, J. F. Mangin, C. Poupon, C. A. Clark, S. Pappata, N. Molko, and H. Chabriat. Diffusion tensor imaging: concepts and applications. *J Magn Reson Imaging*, 13:534–546, Apr 2001.

[6] R. Bammer and F. Fazekas. Diffusion imaging in multiple sclerosis. *Neuroimaging Clin. N. Am.*, 12:71–106, Feb 2002.

[7] EO Stejskal and JE Tanner. Spin diffusion measurements: spin echoes in the presence of a time-dependent field gradient. *Journal of Chemical Physics*, 42(1):288–&, 1965.

[8] A Einstein. The motion of elements suspended in static liquids as claimed in the molecular kinetic theory of heat. *ANNALEN DER PHYSIK*, 17(8):549–560, JUL 1905.

[9] P. J. Basser, J. Mattiello, and D. LeBihan. MR diffusion tensor spectroscopy and imaging. *Biophys. J.*, 66:259–267, Jan 1994.

[10] M. A. Bernstein, K.F King, and J.Z. Xiaohong. *Handbook of MRI Pulse Sequences*. Academic Press; 1 edition, 2004.

[11] M. Cercignani, M. A. Horsfield, F. Agosta, and M. Filippi. Sensitivity-encoded diffusion tensor MR imaging of the cervical cord. *AJNR Am J Neuroradiol*, 24:1254–1256, 2003.

[12] K. Tsuchiya, A. Fujikawa, and Y. Suzuki. Diffusion tractography of the cervical spinal cord by using parallel imaging. *AJNR Am J Neuroradiol*, 26:398–400, Feb 2005.

[13] M. Ries, R. A. Jones, V. Dousset, and C. T. Moonen. Diffusion tensor MRI of the spinal cord. *Magn Reson Med*, 44:884–892, Dec 2000.

[14] P. H. Le Roux, A. Darquie, P. G. Carlier, and C. A. Clark. Feasibility study of non Carr Purcell Meiboom Gill single shot fast spin echo in spinal cord diffusion imaging. *MAGMA*, 14:243–247, Jun 2002.

[15] R. Bammer, M. Augustin, R. W. Prokesch, R. Stollberger, and F. Fazekas. Diffusion-weighted imaging of the spinal cord: interleaved echo-planar imaging is superior to fast spin-echo. *J Magn Reson Imaging*, 15:364–373, Apr 2002.

[16] S. E. Maier and H. Mamata. Diffusion tensor imaging of the spinal cord. *Ann. N. Y. Acad. Sci.*, 1064:50–60, Dec 2005.

[17] C. A. Wheeler-Kingshott, S. J. Hickman, G. J. Parker, O. Ciccarelli, M. R. Symms, D. H. Miller, and G. J. Barker. Investigating cervical spinal cord structure using axial diffusion tensor imaging. *Neuroimage*, 16:93–102, May 2002.

[18] E. K. Jeong, S. E. Kim, J. Guo, E. G. Kholmovski, and D. L. Parker. High-resolution DTI with 2D interleaved multislice reduced FOV single-shot diffusion-weighted EPI (2D ss-rFOV-DWEPI). *Magn Reson Med*, 54:1575–1579, Dec 2005.

[19] R. J. Ogg, P. B. Kingsley, and J. S. Taylor. WET, a T1- and B1-insensitive water-suppression method for in vivo localized 1H NMR spectroscopy. *J Magn Reson B*, 104:1–10, May 1994.

[20] P. Le Roux, R. J. Gilles, G. C. McKinnon, and P. G. Carlier. Optimized outer volume suppression for single-shot fast spin-echo cardiac imaging. *J Magn Reson Imaging*, 8:1022–1032, 1998.

[21] A Volk, B Tiffon, J Mispelter, and JM Lhoste. Chemical shift-specific slice selection - a new method for chemical-shift imaging at high magnetic-field. *J. Magn. Reson.*, 71(1):168–174, Jan 1987.

[22] R. F. Schulte, J. Tsao, P. Boesiger, and K. P. Pruessmann. Equi-ripple design of quadratic-phase RF pulses. *J. Magn. Reson.*, 166:111–122, Jan 2004.

[23] M. Garwood and L. DelaBarre. The return of the frequency sweep: designing adiabatic pulses for contemporary NMR. *J. Magn. Reson.*, 153:155–177, Dec 2001.

[24] J. M. Gomori, G. A. Holland, R. I. Grossman, W. B. Gefter, and R. E. Lenkinski. Fat suppression by section-select gradient reversal on spin-echo MR imaging. Work in progress. *Radiology*, 168:493–495, Aug 1988.

[25] R. Treier, A. Steingoetter, M. Fried, W. Schwizer, and P. Boesiger. On the necessity of flip angle correction for fast T1mapping using DESPOT. *Proc. ISMRM, 14th Scientific Meeting and Exhibition*, page 2264, Mar 2006.

[26] T. Netsch and A. van Muiswinkel. Quantitative evaluation of image-based distortion correction in diffusion tensor imaging. *IEEE Trans Med Imaging*, 23:789–798, Jul 2004.

[27] P. J. Basser. Inferring microstructural features and the physiological state of tissues from diffusion-weighted images. *NMR Biomed*, 8:333–344, 1995.

[28] R. Bammer and F. Fazekas. Diffusion imaging of the human spinal cord and the vertebral column. *Top Magn Reson Imaging*, 14:461–476, Dec 2003.

[29] G. J. Wilson, P. Wang, J. Szumowski, and F. G Hoogenrad. Diffusion-weighted imaging of the spinal cord using sense at 3t. *Proc. ISMRM, 12th Scientific Meeting and Exhibition*, Mar 2004.

[30] K. P. Pruessmann, M. Weiger, M. B. Scheidegger, and P. Boesiger. SENSE: sensitivity encoding for fast MRI. *Magn Reson Med*, 42:952–962, Nov 1999.

[31] C. A. Clark and D. J. Werring. Diffusion tensor imaging in spinal cord: methods and applications - a review. *NMR Biomed*, 15:578–586, 2002.

[32] K. Tsuchiya, S. Katase, A. Fujikawa, J. Hachiya, H. Kanazawa, and K. Yodo. Diffusion-weighted MRI of the cervical spinal cord using a single-shot fast spin-echo technique: findings in normal subjects and in myelomalacia. *Neuroradiology*, 45:90–94, Feb 2003.

[33] S. Rieseberg, K. D. Merboldt, M. Küntzel, and J. Frahm. Diffusion tensor imaging using partial Fourier STEAM MRI with projection onto convex subsets reconstruction. *Magn Reson Med*, 54:486–490, Aug 2005.

[34] U. G. Nolte, J. Finsterbusch, and J. Frahm. Rapid isotropic diffusion mapping without susceptibility artifacts: whole brain studies using diffusion-weighted single-shot STEAM MR imaging. *Magn Reson Med*, 44:731–736, Nov 2000.

[35] A. Demir, M. Ries, C. T. Moonen, J. M. Vital, J. Dehais, P. Arne, J. M. Caillé, and V. Dousset. Diffusion-weighted MR imaging with apparent diffusion coefficient and apparent diffusion tensor maps in cervical spondylotic myelopathy. *Radiology*, 229:37–43, Oct 2003.

[36] P. Summers, P. Staempfli, T. Jaermann, S. Kwiecinski, and S. Kollias. A preliminary study of the effects of trigger timing on diffusion tensor imaging of the human spinal cord. *AJNR Am J Neuroradiol*, 27:1952–1961, Oct 2006.

[37] D. A. Feinberg, J. C. Hoenninger, L. E. Crooks, L. Kaufman, J. C. Watts, and M. Arakawa. Inner volume MR imaging: technical concepts and their application. *Radiology*, 156:743–747, Sep 1985.

[38] C. A. Wheeler-Kingshott, G. J. Parker, M. R. Symms, S. J. Hickman, P. S. Tofts, D. H. Miller, and G. J. Barker. ADC mapping of the human optic nerve: increased resolution, coverage, and reliability with CSF-suppressed ZOOM-EPI. *Magn Reson Med*, 47:24–31, Jan 2002.

[39] P Mansfield, RJ Ordidge, and R Coxon. Zonally Magnified EPI in Real-Time by NMR. *Journal of Physics E-Scientific Instruments*, 21(3):275–280, MAR 1988.

[40] S. Rieseberg, J. Frahm, and J. Finsterbusch. Two-dimensional spatially-selective RF excitation pulses in echo-planar imaging. *Magn Reson Med*, 47:1186–1193, Jun 2002.

[41] B. J. Wilm, J. Svensson, A. Henning, K. P. Pruessmann, P. Boesiger, and S. S. Kollias. Reduced field-of-view MRI using outer volume suppression for spinal cord diffusion imaging. *Magn Reson Med*, 57:625–630, Mar 2007.

[42] C. A. Wheeler-Kingshott, S. A. Trip, M. R. Symms, G. J. Parker, G. J. Barker, and D. H. Miller. In vivo diffusion tensor imaging of the human optic nerve: pilot study in normal controls. *Magn Reson Med*, 56:446–451, Aug 2006.

[43] S. E. Maier. Slab scan diffusion imaging. *Magn Reson Med*, 46:1136–1143, Dec 2001.

[44] M. Oelhafen, K. P. Pruessmann, S. Kozerke, and P. Boesiger. Calibration of echo-planar 2D-selective RF excitation pulses. *Magn Reson Med*, 52:1136–1145, Nov 2004.

[45] C. Reischauer, P. Staempfli, T. Jaermann, S.S. Kollias, and P. Boesiger. Development of a temperature controlled anisotropic diffusion phantom. *Proc. ISMRM, 15th Scientific Meeting and Exhibition*, page 3535, Mar 2007.

[46] H. S. Kharbanda, D. C. Alsop, A. W. Anderson, G. Filardo, and D. B. Hackney. Effects of cord motion on diffusion imaging of the spinal cord. *Magn Reson Med*, 56:334–339, Aug 2006.

[47] D.K. Jones and C. Pierpaoli. Contribution of cardiac pulsation to variability of tracking results. *Proc. ISMRM, 13th Scientific Meeting and Exhibition*, page 222, Mar 2005.

[48] D. Facon, A. Ozanne, P. Fillard, J. F. Lepeintre, C. Tournoux-Facon, and D. Ducreux. MR diffusion tensor imaging and fiber tracking in spinal cord compression. *AJNR Am J Neuroradiol*, 26:1587–1594, 2005.

[49] C. Rossi, A. Boss, G. Steidle, P. Martirosian, U. Klose, S. Capuani, B. Maraviglia, C. D. Claussen, and F. Schick. Water diffusion anisotropy in white and gray matter of the human spinal cord. *J Magn Reson Imaging*, 27:476–482, Mar 2008.

[50] C. Pierpaoli and P. J. Basser. Toward a quantitative assessment of diffusion anisotropy. *Magn Reson Med*, 36:893–906, Dec 1996.

[51] S Kwiecinski, P Summers, Z Hao, A Curt, and S.S. Kollias. In vivo measurements of diffusivity and anisotropy in the human spinal cord: Normative data from healthy controls. In *Abstract in proceedings of the Swiss Society for Neuroscience 2004:56.*, 2004.

[52] S Ramon y Cajal. *Histology of the Nervous System, Chapter XI, Structure of Spinal White Matter.* Oxford University Press, 1995;7:248-284.

[53] G. J. Stanisz, E. E. Odrobina, J. Pun, M. Escaravage, S. J. Graham, M. J. Bronskill, and R. M. Henkelman. T1, T2 relaxation and magnetization transfer in tissue at 3T. *Magn Reson Med*, 54:507–512, Sep 2005.

[54] P Mansfield and B Chapman. Active magnetic screening of coils for static and time-dependent magnetic field generation in NMR imaging. *Journal of Physics E - Scientific Instruments*, 19(7):540–545, JUL 1986.

[55] DJ Jensen, WW Brey, JL Delayre, and PA Narayana. Reduction of Pulsed Gradient Settling Time in the Superconducting Magnet of a Magnetic-Resonance Instrument. *Medical Physics*, 14(5):859–862, SEP-OCT 1987.

[56] G Wider, V Dotsch, and K Wuthrich. Self-Compensating Pulsed Magnetic-Field Gradients For Short Recovery Times. *Journal Of Magnetic Resonance Series A*, 108(2):255–258, JUN 1994.

[57] A. L. Alexander, J. S. Tsuruda, and D. L. Parker. Elimination of eddy current artifacts in diffusion-weighted echo-planar images: the use of bipolar gradients. *Magn Reson Med*, 38:1016–1021, Dec 1997.

[58] MA Morich, DA Lampman, WR Dannels, and FTD Goldie. Exact Temporal Eddy-Current Compensation in Magnetic-Resonance Imaging-Systems. *IEEE Transactions on Medical Imaging*, 7(3):247–254, SEP 1988.

[59] C. Boesch, R. Gruetter, and E. Martin. Temporal and spatial analysis of fields generated by eddy currents in superconducting magnets: optimization of corrections and quantitative characterization of magnet/gradient systems. *Magn Reson Med*, 20:268–284, Aug 1991.

[60] NG Papadakis, KM Martin, JD Pickard, LD Hall, TA Carpenter, and CLH Huang. Gradient preemphasis calibration in diffusion-weighted echo-planar imaging. *Magnetic Resonance in Medicine*, 44(4):616–624, OCT 2000.

[61] RJ Ordidge and ID Cresshull. The correction of transient B0 field shifts following the application of pulsed gradients by phase correction in the time domain. *Journal of Magnetic Resonance*, 69(1):151–155, AUG 1986.

[62] T Ondera, S Matsui, K Sekihara, and H Kohno. A Method of Measuring Field-Gradient Modulation Shapes - Application to high-Speed NMR Spectroscopic Imaging. *Journal of Physics E- Scientific Instruments*, 20(4):416–419, APR 1987.

[63] H.K. Lee, G.C. Kashmar, and O Nalcioglu. A Practical Measure of EPI Gradient Shapes Using the FID Signals. *Proc. ISMRM, Scientific Meeting and Exhibition*, page 1388, Mar 1996.

[64] JH Duyn, YH Yang, JA Frank, and JW van der Veen. Simple correction method for k-space trajectory deviations in MRI. *Journal of Magnetic Resonance*, 132(1):150–153, MAY 1998.

[65] G. F. Mason, T. Harshbarger, H. P. Hetherington, Y. Zhang, G. M. Pohost, and D. B. Twieg. A method to measure arbitrary k-space trajectories for rapid MR imaging. *Magn Reson Med*, 38:492–496, Sep 1997.

[66] M. T. Alley, G. H. Glover, and N. J. Pelc. Gradient characterization using a Fourier-transform technique. *Magn Reson Med*, 39:581–587, Apr 1998.

[67] P. Jezzard, A. S. Barnett, and C. Pierpaoli. Characterization of and correction for eddy current artifacts in echo planar diffusion imaging. *Magn Reson Med*, 39:801–812, May 1998.

[68] P. Börnert, H. Schomberg, B. Aldefeld, and J. Groen. Improvements in spiral MR imaging. *MAGMA*, 9:29–41, Oct 1999.

[69] O Josephs, R Deichmann, and R Turner. Trajectory measurement and generalised reconstruction in rectilinear epi. *NeuroImage*, 11(5, Supplement 1):543–543, 2000.

[70] A. Ebel and A. A. Maudsley. Detection and correction of frequency instabilities for volumetric 1H echo-planar spectroscopic imaging. *Magn Reson Med*, 53:465–469, Feb 2005.

[71] R. Katz-Brull and R. E. Lenkinski. Frame-by-frame PRESS 1H-MRS of the brain at 3 T: the effects of physiological motion. *Magn Reson Med*, 51:184–187, Jan 2004.

[72] C. Barmet, N. De Zanche, and K.P. Pruessmann. Spatiotemporal magnetic field monitoring for MR. *Magn Reson Med*, 60:187–197, Jul 2008.

[73] RV Pound and WD Knight. A Radiofrequency Spectrograph and Simple Magnetic-Field Meter. *Review of Scientific Instruments*, 21(3):219–225, 1950.

[74] D. L. Olson, M. E. Lacey, and J. V. Sweedler. High-resolution microcoil NMR for analysis of mass-limited, nanoliter samples. *Anal. Chem.*, 70:645–650, Feb 1998.

[75] G Boero, J Frounchi, B Furrer, PA Besse, and RS Popovic. Fully integrated probe for proton nuclear magnetic resonance magnetometry. *Review of Scientific Instruments*, 72(6):2764–2768, JUN 2001.

[76] N. De Zanche, C. Barmet, J.A. Nordmeyer-Massner, and K.P. Pruessmann. NMR probes for measuring magnetic fields and field dynamics in MR systems. *Magn Reson Med*, 60:176–186, Jul 2008.

[77] T. L. Peck, R. L. Magin, and P. C. Lauterbur. Design and analysis of microcoils for NMR microscopy. *J Magn Reson B*, 108:114–124, Aug 1995.

[78] B. Behnia and A. G. Webb. Limited-sample NMR using solenoidal microcoils, perfluorocarbon plugs, and capillary spinning. *Anal. Chem.*, 70:5326–5331, Dec 1998.

[79] ME Stoll and TJ Majors. Reduction of Magnetic-Susceptibility Broadening in NMR by Susceptibility Matching. *Journal of Magnetic Resonance*, 46(2):283–288, 1982.

[80] R.M. Bozorth. Ferromagnetism. *Van Nostrand, New York*, 1951.

[81] C. Barmet, N. De Zanche, L.S. Sasportas, and K.P. Pruessmann. A model-free method for high-precision mr susceptometry. *Proc. ISMRM, 15th Scientific Meeting and Exhibition*, page 36, Mar 2007.

[82] G.O. McClurg. Magnetic field distributions for a sphere and for an ellipsoid. *American Journal of Physics*, 24(7):496–499, Oct. 1956.

[83] M Burl and I.R. Young. Eddy currents and their control: The encyclopaedia of nuclear magnetic resonance. *New York: Wiley*, 1996.

[84] S Ramo, JR Whinnery, and T Van Duzer. *Field and Waves in Communication Electronics.* John Wiley & Sons, Inc., New York, 3rd ed, 1994.

[85] C.N. Chen and D.I. Hoult. *Biomedical Magnetic Resonance Technology.* Adam Hilger, Bristol, UK, 1989.

[86] R.C. Hansen. *Phased Array Antennas.* John Wiley and Sons Inc., 1998.

[87] B. Aldefeld and P. Börnert. Effects of gradient anisotropy in MRI. *Magn Reson Med*, 39:606–614, Apr 1998.

[88] A Vlassenbroek, J Jeener, and P Broekaert. Macroscopic and microscopic fields in high-resolution liquid NMR. *Journal of Magnetic Resonance, Series A*, 118(2):234–246, 1996.

[89] D. G. Norris and J. M. Hutchison. Concomitant magnetic field gradients and their effects on imaging at low magnetic field strengths. *Magn Reson Imaging*, 8:33–37, 1990.

[90] KF King, A Ganin, XHJ Zhou, and MA Bernstein. Concomitant gradient field effects in spiral scans. *Magn Reson Med*, 41(1):103–112, JAN 1999.

[91] D. J. Tyler and P. A. Gowland. Rapid quantitation of magnetization transfer using pulsed off-resonance irradiation and echo planar imaging. *Magn Reson Med*, 53:103–109, Jan 2005.

[92] T. G. Reese, O. Heid, R. M. Weisskoff, and V. J. Wedeen. Reduction of eddy-current-induced distortion in diffusion MRI using a twice-refocused spin echo. *Magn Reson Med*, 49:177–182, Jan 2003.

[93] G. K. Rohde, A. S. Barnett, P. J. Basser, S. Marenco, and C. Pierpaoli. Comprehensive approach for correction of motion and distortion in diffusion-weighted MRI. *Magn Reson Med*, 51:103–114, Jan 2004.

[94] C. Barmet, N. De Zanche, and K.P. Pruessmann. A transmit/receive system for magnetic field monitoring of in-vivo mri. *Magn Reson Med*, in press, Jul 2009.

[95] C. Barmet, B.J. Wilm, M. Pavan, and K. Pruessmann. A third-order field camera with microsecond resolution for mr system diagnostics. *Proc. ISMRM, 17th Scientific Meeting and Exhibition*, Mar 2009.

[96] K.P. Pruessmann, M. Weiger, P. Börnert, and P. Boesiger. Advances in sensitivity encoding with arbitrary k-space trajectories. *Magn Reson Med*, 46:638–651, Oct 2001.

[97] E. T. Whittaker and G. N. Watson. *A Course Of Modern Analysis.* Cambridge Mathematical Library, 1973.

[98] A Maeda, K Sano, and T Yokoyama. Reconstruction by weighted correlation for MRI with time-varying gradients. *IEEE Trans Med Imaging*, 7(1):26–31, MAR 1988.

[99] K. Sekihara, S. Matsui, and H. Kohno. NMR imaging for magnets with large nonuniformities. *IEEE Trans Med Imaging*, 4:193–199, 1985.

[100] K.P. Pruessmann and J. Tsao. Minimum norm sense reconstruction for optimal spatial response. *United States Patent*, US2006/0186941 1A, 2006.

[101] DC Noll. Rapid MR image acquisition in the presence of background gradients. In *IEEE International Symposium on Biomedical Imaging, Washington, D.C., Jul 07-10, 2002*, 2002.

[102] P Bachmann. *Analytische Zahlentheorie, Bd. 2 : Die Analytische Zahlentheorie.* Leipzig, Germany: Teubner, 1894.

[103] P. J. Beatty, D. G. Nishimura, and J. M. Pauly. Rapid gridding reconstruction with a minimal oversampling ratio. *IEEE Trans Med Imaging*, 24:799–808, Jun 2005.

[104] YS Zhao, AW Anderson, and JC Gore. Computer simulation studies of the effects of dynamic shimming on susceptibility artifacts in EPI at high field. *JOURNAL OF MAGNETIC RESONANCE*, 173(1):10–22, MAR 2005.

[105] J. Hennig, A. M. Welz, G. Schultz, J. Korvink, Z. Liu, O. Speck, and M. Zaitsev. Parallel imaging in non-bijective, curvilinear magnetic field gradients: a concept study. *MAGMA*, 21:5–14, Mar 2008.

[106] L. C. Man, J. M. Pauly, and A. Macovski. Multifrequency interpolation for fast off-resonance correction. *Magn Reson Med*, 37:785–792, May 1997.

[107] S.S. Stone, J.P. Haldar, Tsao S.C., Hwu W.M.W., Sutton B.P., and Liang Z.P. Accelerating advanced mri reconstructions on gpus. *Journal of Parallel and Distributed Computing*, 68(10):1307–1318, 2008.

[108] J. von Meyenburg, B. Wilm, A. Weck, Gallus E., Schätzle E., P. Boesiger, N. Goebels, and S. S. Kollias. Diffusion tensor mri study of the spinal cord in patients with multiple sclerosis. *Proc. ISMRM, 17th Scientific Meeting and Exhibition*, Mar 2009.

[109] C. Reischauer, B. J. Wilm, J. M. Froehlich, P. Boesiger, and K. U. Wentz. High-resolution diffusion-weighted imaging for the diagnosis of prostate cancer. *Proc. ISMRM, 17th Scientific Meeting and Exhibition*, Mar 2009.

Danksagung

Ich möchte allen danken, die zum Gelingen dieser Dissertation beigetragen haben. Mein besonderer Dank geht an...

- Prof. Dr. Peter Bösiger, der durch seinen ständigen Einsatz ein kreatives und auch herzliches Forschungsumfeld schafft.
- Prof. Dr. med. Spyros Kollias für seinen Weitblick in der medizinschen Forschung und sein grosses Engagement bei allen klinischen Projekten.
- Prof. Dr. Klaas Prüssmann und Dr. Jonas Svensson für die vielen interessanten Diskussionen und Ihre Unterstützung, die wesentlich zu dieser Dissertation beigetragen haben.
- Christoph Barmet, Urs Gamper, Anke Henning, Jan von Meyenburg und Jens Petersen für die konstruktive und freundschaftliche Zusammenarbeit in den gemeinsamen Projekten.
- Roger Lüchinger, Dieter Meier, Urs Sturzenegger und Bruno Willi für Ihren stets raschen technischen Support.
- Marianne Berg, die mir mit vielen administrativen Belangen geholfen hat.
- Allen früheren und derzeitigen Kollegen, Alex, Andrea, Andreas, Ariane, Armin, Astrid, Basti, Betina, Birgit, Carolin, Christian, Christof, Christoph, Conny, David, Diane-Elise, Dorothea, Erin, Florian, Gerard, Hendrik, Jelena, Jochen, Johanna, Johannes, Jurek, Kai, Kilian, Lars, Marco J., Marco P., Martin, Max, Matteo, Michael, Michi, Mike, Moe, Nicola, Philipp, Reto, Robert M., Robert V.,

Rudolf, Salome, Stigi, Susanne, Thomas L., Thomas J., Tobias, Verena, Victor, Viton, Xing, Xinhui für die diskussionfreudige und offene Athmosphäere am Institut.

Curriculum Vitae

I was born on July 4^{th} 1979 in Graz (Austria) as the 2^{nd} child of Friedrich and Sylvia Wilm. I grew up in Munich (Germany), where I attended primary school. In the same place I attended the Maria-Theresia-Gymnasium, from where I graduated in May 1998 (Abitur).
I started my studies in Computer Science (Informatik) at the Technical University Munich (Germany) in October 1998. In 2001, I spent one semester as an exchange student at the National University of Singapore (Singapore). After my diploma thesis at the Institute of Computer Vision, I graduated from the TU Munich with a diploma in Computer Science in February 2004.
In August 2004, I joined the bio-physics group of Prof. P. Bösiger at the Institute for Biomedical Engineering, University and ETH Zurich (Switzerland), as a PhD student and research assistant.